# Energy Advances

## Accepted Manuscript

This article can be cited before page numbers have been issued, to do this please use: Y. Shen, Z. Zhu, Z. Xu and Y. Li, *Energy Adv.*, 2024, DOI: 10.1039/D4YA00209A.




ROYAL SOCIETY OF CHEMISTRY

rsc.li/energy-advances

View Article Online
DOI: 10.1039/D4YA00209A

# Data availability statements

No primary research results, software or code have been included and no new data were generated or analysed as part of this review.



View Article Online
DOI: 10.1039/D4YA00209A

ARTICLE

# Recent progress of 2D inorganic non-conductive materials for alkali metal based batteries

Received 00th January 20xx,
Accepted 00th January 20xx

DOI: 10.1039/x0xx00000x

Yuxi Shen, Zengquan Zhu, Zhefeng Xu,* Yueming Li*

The urgent need for developing energy storage devices is promoting the studies of alkaline metal based batteries with high energy density and long life. Two-dimensional (2D) inorganic non-conductive materials have shown their unique physicochemical properties, making them great potential in energy storage and conversion due to the planar structure, high surface-to-volume ratio, and non-electronic conductivity. Among the 2D inorganic non-conductive materials, hexagonal boron nitride (h-BN), graphitic nitride(g-$C_3N_4$), montmorillonite (MMT), and vermiculite (VMT) have shown some potential application in alkaline metal based batteries. Herein, the synthesis strategies of these inorganic two-dimensional non-conductive materials in recent years and their applications as electrode materials additives, metal anode supports, building block of solid interfacial and separator additives in alkali metal based batteries are comprehensively reviewed in recent years. The challenges of using 2D materials in alkali metal based to improve performance are discussed and possible solutions are proposed. These 2D inorganic non-conductive materials have the potential to get broader usage in alkali-based batteries in future considering their unique structure and properties.

## 1. Introduction

The development of renewable energy is paramount in addressing energy depletion and environmental pollution. However, the instability and volatility of renewable energy sources can bring a significant challenge in terms of energy storage. Rechargeable batteries are widely employed to store renewable energy and bridge the gap between supply and demand.[1] Among these, lithium-ion batteries (LIBs) as one type of alkali metal based batteries have emerged as one of the most commonly used energy storage solutions due to their high energy density, long cycle life, and low self-discharge rate. Nevertheless, with the rapid development of electric vehicles and portable electronic devices, the demand for higher battery energy density and extended driving range has grown, pushing traditional LIBs close to their limits. As a result, researchers have turned their attention to next-generation battery technologies with higher theoretical energy densities.

Besides LIBs, other alkali metal based batteries such as Li-metal, Li/Na-$O_2$, Li-S, and Na/K metal batteries have been paid much attention due to higher specific capacity, and lower costs. Lithium metal batteries (LMBs) have received significant research and exploration, in which lithium metal is used as the anode material, being able to offer higher theoretical energy density. As is known, lithium metal has a lightweight (0.59 g $cm^{-3}$), low reduction potential (–3.04 V vs. the standard hydrogen electrode), and high theoretical specific capacity (3860 mAh $g^{-}1$). However, LMBs face multiple challenges such as lithium dendrite formation and electrolyte decomposition, needing necessary improvements for practical application.[2] Another promising type of alkaline based battery is lithium-sulfur (Li-S) batteries[3] because of the high theoretical capacity and abundant resources of sulfur element. However, Li-S batteries also face challenges such as the shuttle of polysulfide shuttle and the low conductivity of the S element, which need to be addressed to achieve reliable commercialization. Additionally, lithium-oxygen (Li-$O_2$) batteries (LOBs) are considered a potential high-energy-density energy storage device.[4] LOBs utilize oxygen gas as the cathode active material, enabling higher theoretical energy density. However, LOBs face challenges related to the formation of solid oxide byproducts, and catalytic efficiency of the oxygen electrode. Even without considering scientific issues, the large-scale application of lithium based batteries will be restricted by the limited and uneven distribution of lithium reserves. To deal with this, researchers have begun to study sodium-ion batteries (SIBs) [5,6] and potassium-ion batteries (PIBs) [7] as cost-effective alternatives to LIBs. Sodium and potassium elements with rich resources, exhibit similar chemical properties and ion transport mechanisms, making them potential substitutes for LIBs.

SIBs may exhibit poor kinetic characteristics due to the larger radius of Na ions during their insertion into the host structure, which can result in the degradation of the host material. In addition, the lower Lewis acidity of sodium complexes leads to higher solubility of solid-electrolyte interphase (SEI), which can result in incomplete coverage of the electrode surface and

[a] State Key Laboratory of Metastable Materials Science and Technology, College of Materials Science and Engineering, Yanshan University, Qinhuangdao 066004, China
Prof. Yueming Li, Email:liyueming@ysu.edu.cn; Dr. Zhefeng Xu, Email:zfxu@ysu.edu.cn

† Footnotes relating to the title and/or authors should appear here.
Electronic Supplementary Information (ESI) available: [details of any supplementary information available should be included here]. See DOI: 10.1039/x0xx00000x

some detrimental side reactions, accelerating heat generation. Furthermore, the cathode materials currently used, including oxides, poly-anions, organics, Prussian blue, and its analogs, all suffer from poor electronic/ion conductivity.[5] In addition, although the use of sodium metal as the anode can solve the issues of poor kinetic insertion of $Na^+$ ions and low capacity, it faces a similar dilemma as lithium metal anode. During the cycling process, the reaction between the sodium metal and the electrolyte continuously increases the interface impedance and consumes the electrolyte, leading to a continuous decrease in the Coulombic efficiency during the charge-discharge process. Furthermore, the formation of a large number of sodium dendrites on the anode surface and the generation of "dead sodium" also reduce the cycling stability. If the further growth of sodium dendrites may penetrate the separator, leading to short circuits and even explosions. [8]

Potassium possesses a standard hydrogen electrode potential (−2.936 V vs SHE) that falls between lithium and sodium. Additionally, potassium ions have smaller solvation shells compared to lithium and sodium ions, resulting in higher ionic conductivity and solubility. However, as research in this field is still in its early stages, potassium-ion batteries face similar challenges to SIBs. The insertion of larger potassium ions causes more significant volume changes in electrode materials during charge-discharge processes compared to other alkali metal ion batteries, leading to unstable electrode structures. [7, 9] Additionally, the low diffusion rate of $K^+$ in solid electrode materials limits its rate performance. Similarly, the lower potential and higher capacity make potassium metal an attractive candidate as a negative electrode for potassium batteries. However, potassium metal electrodes also face challenges with dendritic growth. Furthermore, the incompatibility of K metal and routine copper foil current collectors presents another significant obstacle to its development.[10] Studies have shown that the modification of electrode materials is very helpful in addressing the issues in these batteries.

As is known, inorganic materials play a critical role in alkaline metal-based batteries. For example, the common commercial LIBs use graphite as anode and $LiNi_xCo_yMn_z$ as cathode. Some inorganic materials have shown the unique role in alkali metal/ion batteries. As an example, sodium trisilicate can be used as electrode binder to produce rigid, load-bearing batteries due to its high strength and stiffness.[11]

Two-dimensional (2D) inorganic non-conductive materials with unique properties are expected to be one of the key materials in improving the batteries performance. The 2D inorganic materials can be divided into conductive materials, semi-conductive materials, and insulators based on their electronic conductivity. Representative examples of conductive 2D inorganic materials include graphene, MXenes ($M_{n+1}AX_n$),[12] and black phosphorus (BP) nanosheets. However, sometimes it is difficult to distinguish between insulators and wide-gap semiconductors, and thus these materials can be classified as non-conductive materials. There are also various inorganic non-conductive 2D materials such as metal hydroxide[13], BN,[14] graphitic carbon nitride ($C_3N_4$),[15] MMT, and VMT.[16]

In fact, non conductive 2D inorganic materials can contribute a lot as additives for SEI, separator, or electrolyte. Although the synthesis of non-conductive 2D nanosheets have been summarized in previous reports,[14, 17-19] there are few reviews on the recent progress of 2D non-conductive inorganic materials as functional additives in alkali metal based batteries.

Herein, we have provided an overview of the typical 2D inorganic non-conductive materials, including BN, g-$C_3N_4$, MMT, and VMT in recent years, and their application in alkali metal based batteries. We will discuss their synthesis and fundamental properties briefly. And then, we will emphasize their applications in alkali metal based batteries, such as Li/Na/K-ion batteries, Li/Na/K-metal batteries, and Li-S/O batteries, shown in Figure 1.

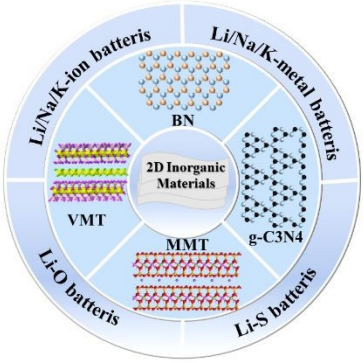


**Figure 1.** Schematic Diagrams of the structure of representative 2D inorganic non-conductive materials and their application in Various Alkali Metal Based Batteries

## 2. Overview of 2D inorganic non-conductive materials

### 2.1. Basic properties of representative 2D materials

2D inorganic non-conductive materials are a class of nanomaterials with ultrathin thickness and much larger lateral size. Their unique geometric structures provide them with unique merits including large specific surface area, short diffusion path of carrier ion, and rich surface chemistry. Additionally, the interlayer covalent bonds in 2D planes ensure adequate mechanical strength. The 2D materials can be prepared by exfoliation of layered materials. 2D inorganic non-conductive materials can be used as building block of other micro/nano structures, making them suitable to be applied in various energy storage fields. Furthermore, the wide bandgap of 2D inorganic non-conductive materials makes them favourable to be used as key components in passivation layer.

#### 2.1.1 Basic properties of hexagonal BN

There are multiple allotropes for boron nitride, and hexagonal boron nitride (h-BN) and cubic boron nitride (c-BN) among them, are more stable compared to others.[20] h-BN is a layered hexagonal crystal, with a structure analogous to graphite. It belongs to the $P6_3/mmc$ space group, with lattice parameters of a = 2.505 Å and c = 6.653 Å. The B and N atoms are bonded through in-plane connections, forming a hexagonal lattice, and

multiple layers stack to create large h-BN crystals.[21] Thanks to the $sp^2$ bonding, the B-N bonds within the plane exhibit remarkable in-plane thermal conductivity, chemical stability, and strength. Due to the layered structure, h-BN bulk materials can be exfoliated into BN nanosheets. The bulk modulus of a single layer of h-BN is approximately 160 GPa, while the bending modulus is around 31.2 GPa. The presence of empty π orbitals renders h-BN an electrical insulator, with an energy bandgap of approximately 5.955 eV.[21-23] The ionic nature of the B-N bonds results in layer-to-layer interactions, leading to an AA' stacking configuration where each N atom is directly above the B atoms of the subsequent layer. In addition to AA' stacking, energetically higher AB stacking (Bernal stacking) is occasionally observed in thin h-BN films.[24-27]

The unique structure of BN has led to its unique properties such as high chemical stability, strong mechanical strength, special optical properties, and special optoelectronic properties.

**2.1.2 Basic properties of g-$C_3N_4$**

Graphitic carbon nitride (g-$C_3N_4$) exhibits a planar two-dimensional layered structure resembling graphene, with carbon and nitrogen atoms in a $sp^2$ conjugated configuration, forming a hexagonal structure, shown in Figure 2.[28] This structure consisting of six atoms is referred to as a triazine ring. Each triazine ring is linked to the adjacent unit through C-N bonds. Currently, it is widely believed that g-$C_3N_4$ may have one of two chemical frameworks: g-CN with triazine rings ($C_3N_3$), which is a part of the $R_3m$ space group, or g-CN with 3-s-triazine rings ($C_6N_7$), which is a part of the $P6m^2$ space cluster.[29] Within g-$C_3N_4$, each triazine ring is connected to the next one via a terminal nitrogen ion, resulting in a homogeneous structure capable of infinite growth. Subsequent experimental and computational analyses have indicated that g-$C_3N_4$ composed of triazine rings as the fundamental unit is more stable than the structure composed of 3-s-triazine rings. During the preparation process, g-$C_3N_4$ can be controllably adjusted to adopt 0D, 1D, 2D, and 3D morphologies.[30] Generally, 0D structured g-$C_3N_4$ exhibits significant size quantization effects, surface effects, and quantum confinement effects. For 1D structured g-$C_3N_4$ (mainly nanotubes and nanofibers), it provides a direct pathway for electron transfer. The interconnected structure of 3D g-$C_3N_4$ allows for good porous channels, rapid electron transfer, larger specific surface area, and more active sites. Additionally, the two surfaces of the two-dimensional nanosheets possess expansive specific surface areas and abundant exposed surface sites.[31] Due to the special structure, g-$C_3N_4$ displays tunable optoelectronic properties.[32]

**2.1.3 Clay-based 2D materials**

Montmorillonite (MMT) belongs to the natural smectite group, which is a layered silicate mineral with a layered structure and high mechanical properties, as shown in Figure 2(e).[33] The composition can be expressed as $[(Na,Ca)_{0.33}(Al, Mg)_2(Si_4O_{10})(OH)_2{\cdot}nH_2O]$. The basic molecular structure is composed of silica tetrahedra and aluminum octahedral units. The $Si^{4+}$ cation has tetrahedral coordination with oxygen, while the $Al^{3+}$ cation has six-fold or octahedral coordination with oxygen.[34] MMT consists of two layers of O-Si-O tetrahedral silicate sheets sandwiching an alumina layer, forming a 2:1 clay with O-Al (Mg)-O octahedral sheets. The silica layers form a hexagonal network by sharing three corners with adjacent tetrahedra.[35] The remaining fourth corner of each tetrahedron is connected to adjacent octahedral sheets. Aluminum or magnesium, coordinated with oxygen and hydroxyl groups from the tetrahedral layer, form the octahedral layers. With the help of van der Waals and electrostatic forces, or through hydrogen bonding, neighboring layers of approximately 10μm in size stack together to form the basic particles of MMT.[36] Additionally, the isomorphous substitution of part of the $Al^{3+}$ in the octahedral sheets with divalent metal cations such as $Mg^{2+}$ and $Fe^{2+}$ or other lower charge cations leads to the charge deficiency of the MMT layers. To balance the charge deficiency, interlayer cations can be exchanged with other metal cations.[37, 38]

Vermiculite (VMT) is a common layered silicate mineral that is characterized by its natural, non-toxic, high expansion, and load-bearing properties. It is a primary product of low-temperature hydrothermal alteration of biotite and phlogopite micas.[39, 40] VMT is formed by the progressive transformation of the original mica. Monolayer VMT has a typical 2:1 structure, composed of two layers of silicon-oxygen tetrahedra sandwiching a layer of magnesium-oxygen octahedral, shown in Figure 2(f).[41] The thickness of a monolayer VMT is approximately 1 nm, with an interlayer spacing of about 1.4 nm.[20] Due to the substitution of aluminum for a portion of silicon in the silicate layers, VMT layers carry a negative charge.[42] Therefore, there are numerous cations, such as $K^+$, $Mg^{2+}$, and $Ca^{2+}$, present in the interlayer space of VMT to maintain charge balance.[42] VMT exhibits a unique characteristic of volume expansion upon heating at elevated temperatures.[44] Expanded VMT possesses excellent properties such as lightweight, low thermal conductivity, insulation, sound absorption, and adsorption.[19, 45] Furthermore, Delaminated VMT nanosheets have a larger specific surface area than expanded VMT due to the exposed interlayer surfaces after delamination.[46-50] Thus, the fresh surface of delaminated VMT nanosheets possesses abundant reactive sites, contributing to significantly higher reactivity compared to expanded VMT. Moreover, VMT nanosheets exhibit a high concentration of negative charges on their surfaces, providing excellent electrical conductivity compared to expanded VMT.[51]

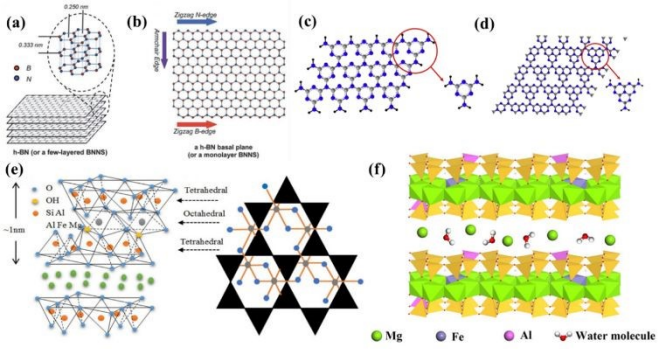


**Figure 2. (a)** Layered van der Waals structure of bulk h-BN and **(b)** planar view of an atomically thin sheet of $sp^2$-bonded B and N atoms that comprise the h-BN crystal or BN nanosheets (BNNS). Adapted with permission.[52] Copyright 2012, The Royal Society of Chemistry. The stacking 2D layering composition, the fundamental constituent elements

are **(c)** s-triazine and **(d)** tri-s-triazine of g-$C_3N_4$. [53] Copyright 2017, Elsevier. **(e)** Schematic representation of the MMT structure.[54] Copyright 2021, Multidisciplinary Digital Publishing Institute. **(f)** Schematic diagram of VMT structure. [19] Copyright 2021, Elsevier.

The single layer of VMT has a typical 2:1 structure, which consists of two layers of silicon oxygen tetrahedron sandwiched by a layer of magnesium oxygen octahedron. There are many cations, such as $K^+$, $Mg^{2+}$, $Ca^{2+}$, and so on, in the interlayer of VMT to maintain electrical balance.[19]

## 2.2. Preparation methods of 2D non-conductive materials

### 2.2.1 Synthesis of BN nanosheets

There are multiple methods, which can be used to prepare h-BN nanosheets. These methods can be divided into two categories: top-down process and bottom-up process. Top-down processes mainly include liquid phase exfoliation, and mechanical exfoliation, while bottom-up processes include physical vapor deposition, solvothermal synthesis, laser plasma deposition, chemical vapor deposition, vapor-liquid-solid growth, and molecular beam epitaxy growth. [20] The detailed synthesis methods have been introduced in previous reports. A typical bottom-up growth process of h-BN involves initial annealing and treatment of the substrate/catalyst, followed by exposure to precursors containing B and N compounds at high temperatures. The catalytic substrate promotes the decomposition of surface precursors and the nucleation and growth of h-BN.[27,55-70] For example, h-BN can be directly grown on $SiO_2$ substrates using low-pressure chemical vapor deposition (LPCVD) with solid ammonia borane precursors or Ru (0001) surface via CVD method., resulting in h-BN films with thicknesses of dozens of nanometers. (Figure 3 (a-c))[71-74]

### 2.2.2 Synthesis of g-$C_3N_4$

Similar to h-BN, both top-down and bottom-up approaches can be applied to prepare 2D g-$C_3N_4$. A lot of methods including the template method, sol-gel method, and exfoliation method can be used to prepare graphitic carbon nitride. Wang et al.[75] have summarized the recent advances in preparation and application in the environment of g-$C_3N_4$ based materials. The preparation of g-$C_3N_4$ nanoparticles (NPs) involves the heating convection of various N-containing organic compounds, including melamine, urea, thiourea, cyanamide, dicyandiamide, etc. [30,78-85]. The top-down approach utilizes methods such as thermal oxidation, ultrasonic treatment, and chemical etching to exfoliate g-$C_3N_4$ into ultrathin sheets. The bottom-up approach involves the direct synthesis of g-$C_3N_4$ nanosheets using nitrogen-rich precursors, templates, or intermolecular interactions.[83] An example of the top-down method was shown in Figure 3(d), in which Niu et al.[84] prepared g-$C_3N_4$ by exfoliation of bulk g-$C_3N_4$ via thermal oxidation The top-down approach allows for the exfoliation of bulk materials into g-$C_3N_4$ nanosheets, but it should be noted that the thinnest material does not necessarily guarantee the best performance.[82] For the bottom-up approach, Kang et al.[85] prepared highly dispersed g-$C_3N_4$ nanosheets with a thickness of approximately 2-3 nm by in-situ direct thermal decomposition of $NH_4HSO_4$ and melamine in air.[86] Additionally, Zhang et al.[87] first prepared ultrathin graphite-like $C_3N_4$ (g-$C_3N_4$) nanosheets from bulk g-$C_3N_4$ in water via a "green" liquid exfoliation route. The resulting ultrathin g-$C_3N_4$ nanosheet solution is highly stable in acidic and alkaline environments and exhibits pH-dependent photoluminescence (PL). (Figure 3(e))

View Article Online
DOI: 10.1039/D4YA00099A

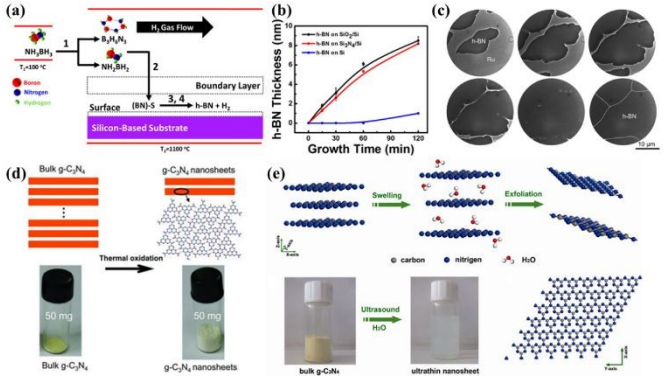


**Figure 3. (a)** Schematic of h-BN growth process. **(b)** Variations of h-BN film thickness at different CVD growth times for $Si_3N_4$/Si, $SiO_2$/Si, and Si substrates.[72] Copyright 2017, American Chemical Society. **(c)** LEEM images of different stages of h-BN growth on Ru(0001) via CVD.[73] Copyright 2011, American Chemical Society. **(d)** Schematic of the structures of the bulk g-$C_3N_4$ and the g-$C_3N_4$ nanosheets. A volume comparison of 50 mg powder of bulk g-$C_3N_4$ and g-$C_3N_4$ nanosheets is given.[83] Copyright 2012, Wiley-VCH. **(e)** Schematic diagram of g-C3N4 preparation, physical image, and perfect crystal structure diagram.[86] Copyright 2012, American Chemical Society.

### 2.2.3 Synthesis of 2D clay nanosheets

#### 2.2.3.1 Synthesis of 2D MMT

According to the previous context, it is known that the interlayer cations of MMT can be exchanged with other metal/organic cations. And the ion exchange is the most commonly applied modification method to prepare 2D MMT nanosheets. For example, Yang et al.[88] prepared lithium-intercalated MMT (Li-MMT) by adding commercial calcium-based MMT and $Li_2CO_3$ to distilled water, shown in Figure 4(a). Hu et al.[89] employed a similar method to modify sodium-based MMT with hexadecyltrimethylammonium bromide (CTAB) to obtain CTAB-MMT, in Figure 4(b). Specifically, during the pretreatment of the original MMT, the slurry was first subjected to low-speed centrifugation, and then the upper suspension was centrifuged further at high speed to obtain thinner MMT flakes. Using this ion exchange strategy, carbon intercalated[90] and $FeS_2$ intercalated MMT[91] can be prepared.

#### 2.2.3.2 Synthesis of 2D VMT nanosheets

VMT also belongs to one kind of natural hydrate clay mineral. VMT is composed of multiple-lamella (silicon-oxygen tetrahedron) and intercalated ions.[92] These 2D nanosheets form three-dimensional structures through weak interlayer interactions such as hydrogen bonds and van der Waals forces.[47] Therefore, by weakening the interlayer interactions in the VMT interlayer space and increasing the interlayer spacing, VMT can be exfoliated into two-dimensional nanosheets.[93] Thus, there is a close relationship between the expansion and exfoliation mechanisms of VMT.

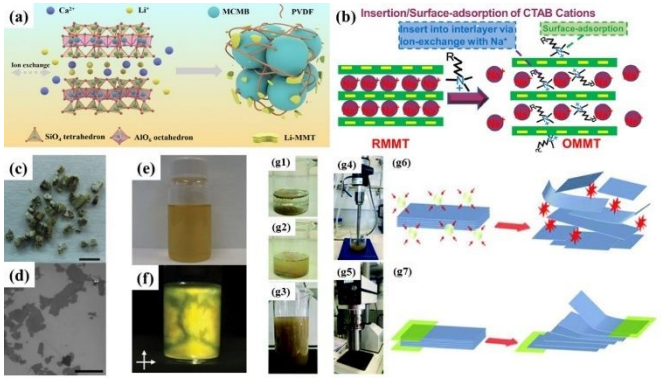


**Figure 4 (a)** The schematic illustration of the synergistic protection of MCMB by Li MMT and PVDF.[88] Copyright 2022, The Royal Society of Chemistry. **(b)** Schematic of insertion/surface-adsorption of CTAB cations for OMMT.[89] Copyright 2022, Elsevier. **(c)** Thermally expanded vermiculite crystals (scale bar, 5 mm), which can be exfoliated by ion exchange to form **(d)** SEM (scale bar, 50 nm). **(e)** a single to few-layer dispersion in water. **(f)** The dispersion exhibits strong birefringence when viewed through crossed polarizers, suggesting nematic ordering originating from the high aspect ratios of the flakes.[48] Copyright 2015, Springer Nature. **(g)** Physical and schematic diagram of ultrasonic and shear force preparation of expanded vermiculite.[94] Copyright 2018, The Royal Society of Chemistry.

The difference between VMT exfoliation and expansion primarily lies in the degree of weakening of the interlayer interactions in VMT. When the interlayer interactions are weakened to a certain extent, VMT undergoes exfoliation. VMT can be exfoliated into monolayer nanosheets with diameters ranging from tens to hundreds of nanometers. Furthermore, the thickness of VMT nanosheets typically consists of only a few atomic layers.[94] The general approaches for preparing exfoliated VMT nanosheets include chemical treatment, mechanical treatment, and combinations of both methods.[48] Figure 4c-g shows two typical examples to prepare 2D VMT nanosheets. [95]

## 3. 2D inorganic materials in alkali metal based batteries

### 3.1. Application of h-BN in alkali metal based Batteries

The 2D non-conductive materials can hardly be used as electrode materials directly due to the poor capability of electron transfer. However, they can be used as additives in electrode materials, separators, and electrolytes because of their unique structure. As batteries are complex systems composed of multiple components including electrode materials, electrolytes, separators, and SEI layer, the modification of the individual component is expected to effectively enhance the overall battery performance. On one hand, conductive 2D inorganic materials can significantly enhance the electrochemical performance of electrode materials. On the other hand, the components in batteries such as separators and SEI layers require materials with non-conductive properties. Goodenough et al.[96] proposed that the stable window of the electrolyte can be evaluated by the following equation.

$E_g=E_{LUMO}-E_{HOMO}$.

(Where $E_{LUMO}$ and $E_{HOMO}$ correspond to the voltages of the lowest unoccupied molecular orbital (LUMO) and the highest occupied molecular orbital (HOMO) of the electrolyte, respectively.) When the chemical potential of the anode ($\mu_a$) is greater than $E_{LUMO}$ ($\mu_a > E_{LUMO}$), electrons tend to transfer from the anode to the electrolyte LUMO conduction band, thereby reducing $E_{LUMO}$, this widens the stable window of the electrolyte. Additionally, the formation of a SEI layer on the negative electrode can extend the stable window, but the formation of the SEI layer results in irreversible lithium consumption. Therefore, pre-assembling an artificial SEI layer on the negative electrode of the battery can effectively widen the stable window of the electrolyte and reduce the irreversible lithium consumption during SEI layer formation. Additionally, the separator, as a crucial component of the battery, serves to isolate the cathode and anode while containing the electrolyte, thus facilitating ion transport. The failure of the membrane can have severe consequences for the battery.

Separators play a vital role in batteries. The separator should possess the following characteristics to ensure proper operation of batteries: (1) excellent chemical stability and compatibility to prevent reactions with other battery components and ensure compatibility with the electrolyte; (2) outstanding mechanical strength to maintain the integrity of the separator and prevent dendrite penetration; (3) good thermal stability to avoid significant shrinkage at high temperatures, and (4) good ion permeability to facilitate rapid ion transport. The thermal stability of commercial PP or PE separators should be further enhanced, thus coating inorganic materials on the surface of these separators has been proven an effective method to improve the thermal stability. [97]

#### 3.1.1 Alkali-ion batteries

##### 3.1.1.1 Electrode material additives

As the extensively used and commercially available alkali battery, LIBs mainly use graphite as an anode, but they suffer from a lack of safety and a low theoretical capacity. Graphene nanosheets can be as anode materials with a higher capacity in LIBs, however, their cycling stability is poor. Li et al.[98] prepared reduced graphene oxide (rGO)/nitride boron thin films through a simple vacuum filtration followed by thermal treatment. (Figure 5(a) Thanks to the unique structure of the rGO/h-BN thin films and the synergistic effect between the layered BN and graphene, the electrolyte penetration was accelerated, and the volume expansion during lithiation and delithiation was buffered. Therefore, the prepared rGO/BN binde-free film with 2wt.% BN content exhibited high reversible capacity, high rate capability, and high capacity retention during the first 200 cycles, achieving a capacity of 278 mAh $g^{-1}$ at 100 mA $g^{-1}$ as anode in LIBs. (Figure 5(b) Due to the 2D structure of BN nanosheets, porous carbon can be embedded in BN nanosheets using MOF-5 as a carbon precursor.[99] The prepared composites demonstrated good cycling stability and high specific capacity characteristics. The improved electrochemical performance was attributed to the high specific surface area of 1790 $m^2$ $g^{-1}$ and enhanced ionic transport, which was caused by the introduction of BN nanosheets.

As an important member of the alkali metal ion battery family, SIBs have become a strong competitor to LIBs due to their richer

availability of sodium resources in nature, moderate energy density, and power density. Datta et al.[100] demonstrated through density functional theory (DFT) calculations that the adsorption energy of Li/Na in the hetero-structures of h-BN and black phosphorus is significantly higher than the cohesive energy of the metals. This ensures that alkali metal aggregation is avoided within the anode material, leading to enhanced cycling stability. Additionally, the atomic incorporation of Li/Na results in an upward shift of the Fermi level in the hetero-structures, facilitating the transition from a semiconductor to a metal and subsequently improving the conductivity. Regarding blue phosphorene, which has similar properties to black phosphorene. (Figure 5(d-i)) Tian et al.[101] demonstrated via calculations that when it forms a heterostructure with h-BN, it can achieve a high theoretical capacity of 801 and 504 mAh $g^{-1}$ for LIBs and SIBs, respectively.

Through DFT calculation, Ahuja et al.[102] demonstrated that introducing vacancy defects into the h-BN monolayer can effectively reduce its bandgap width. When $Li^+$, $Na^+$, or $K^+$ are adsorbed, the bandgap width disappears, displaying metallic properties. The maximum theoretical capacity of alkali metal ions adsorbed on the h-BN monolayer reaches up to 762, 572 and 127 mAh $g^{-1}$ for Li, Na, and K, respectively, however, these materials themselves can hardly be used as anode materials due to the poor electronic conductivity.

#### 3.1.1.2 Separators additives

As one of the most critical components of LIBs, the separator does not directly participate in the electrochemical reaction inside the battery. However, it can prevent contact between the electrodes to avoid internal short circuits, store the liquid electrolyte, and ensure efficient ion transport during charging and discharging. However, the commonly used polymer separators, such as polyethylene (PE) and polypropylene (PP), have poor thermal stability at high temperatures in LIBs. Considering the excellent thermal stability and non-conductive nature, 2D h-BN nanosheets are very promising in addressing the poor thermal stability of traditional polymer separators. He et al.[103] fabricated a bilayer separator by incorporating BN and LaO into a Poly (vinylidene fluoride-hexafluoropropylene) (PVH) matrix through roll-pressing. (Figure 5(j) The incorporation of h-BN showed a strong interfacial interaction with the PVH matrix, greatly enhancing the mechanical strength and thermal stability of the separator. As a result, the bilayer separator with a thickness of 25 µm only shrank by 5.2% after annealing at 150 °C for 1 hour, whereas the shrinkage rate of the commercial Celgard 2325 separator was as high as 40%. Furthermore, in another study by their team, [104] it was demonstrated that h-BN has strong adsorption energy and a large interaction area with polymers, which can prevent the delamination of bilayer organic separators and lead to improved overall performance.

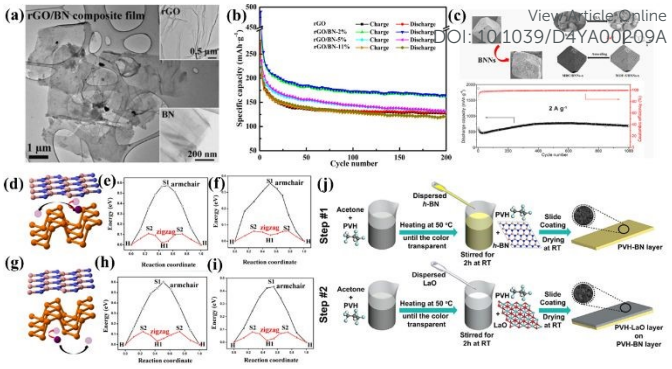


**Figure 5. (a)** TEM images of the prepared rGO/BN-2% composite film, and rGO and BN. **(b)** Cycling performance for different separators.[98] Copyright 2015, Elsevier. **(c)** Illustration of the synthesis pathway of MOF-5/BNNs-x, and the cycling performance.[99] Copyright 2021, Elsevier. Schematic representation of the diffusion path of alkali **(d)** along the intercalated region between the h-BN and Pn layers and (g) above the surface of the Pn layer, the diffusion barrier for **(e)** Li and **(f)** Na along the armchair and zigzag pathways in the intercalated region, the diffusion barrier for (h) Li and (i) Na along the armchair and zigzag pathway over the Pn surface.[100] Copyright 2016, American Chemical Society. **(j)** Schematic illustration of preparation of bi-layer separator.[103] Copyright 2019, Elsevier.

### 3.1.2 Alkali-metal batteries

#### 3.1.2.1 Additives for metal surface modification

LMBs are very promising based on their high energy density in the future. However, the uncontrollable growth of lithium dendrites and volume expansion during lithium plating/stripping processes have hindered the application. The high mechanical strength and thermal stability of h-BN are considered capable of restricting lithium dendrite growth and have therefore been widely used in the modification of lithium metal anodes. Zhu et al.[105] *in-situ* exfoliated bulk BN into BN nanosheets using lignosulfonate (SL) and prepared a layered porous SL/BN three-dimensional composite substrate using a freeze-casting method. The exfoliated BN nanosheets effectively regulated the temperature distribution and induced uniform lithium deposition. The generation of lithium dendrites was effectively suppressed during the lithium plating/stripping process, achieving stable cycling for 500 hours at 4 mA $cm^{-2}$. Li et al. [106] improved the performance of LMB by introducing h-BN in Li-Zn alloy. They proposed that the uniformly distributed h-BN in the anode leads to strong electrokinetic effects due to the high Zeta potential, resulting in a fast transport of Li-ions. Furthermore, h-BN is found to be able to change the interface between lithium metal and solid state electrolyte. For instance, Huang et al.[107] constructed a Li-BN nanosheet composite anode by adding only 5 wt% of BN nanosheets to lithium metal, triggering the transition from point contact to complete adhesion between Li metal and ceramic solid-state electrolytes, greatly reducing the interface resistance between the electrode and the electrolyte, and thereby improving the electrochemical performance.

#### 3.1.2.2 Building block of artificial SEI layer

Due to the high chemical reactivity of lithium metal, it easily reacts with the electrolyte to form a SEI layer. During subsequent cycling, uneven lithium deposition can lead to the growth of lithium dendrites and volume expansion, resulting in the rupture of the original SEI layer. This causes the growing

View Article Online DOI: 10.1039/D4YA00209A



lithium dendrites to contact the electrolyte again, forming a new SEI, which then fractures and regenerates in the following cycles. This further promotes the growth of lithium dendrites and consumption of the electrolyte, significantly reducing the Coulombic efficiency of LMBs. Previous studies have shown that the adsorption energies of Li atoms on the (001) and (110) planes of lithium metal surfaces are −1.68 and −1.85 eV, respectively, far greater than their adsorption energy on the h-BN surface (−0.56 eV).[108] According to the calculation, h-BN can effectively block electron transfer to the electrolyte. Therefore, lithium will hardly deposit on the surface of h-BN. The introduction of h-BN can lower the migration barriers. The low lithium migration energy barrier and high stiffness of the h-BN film can synergistically promote the uniform distribution of lithium underneath the h-BN film, induce a hierarchical growth mechanism of the hidden lithium metal layer, and suppress the growth of lithium dendrites.

As the building block of artificial SEI, this boron nitride material can be used alone or in combination with other materials. Cui et al.[109] deposited a layer of h-BN film on a copper foil surface using chemical vapor deposition (CVD) and slurry coating. It is found that both methods can reduce the deposition energy barrier due to the excellent chemical stability, mechanical strength, and flexibility of h-BN, shown in Figure 6a. Tian et al.[110] used pulsed laser deposition (PLD) to construct a 3D hairball-shaped h-BN structure consisting of nanosheets on the lithium metal anode, in which the stable and highly mechanically resistant h-BN coating can serve as an interfacial layer. Due to the flexibility of the h-BN coating and its ability to effectively alleviate the decomposition of the electrolyte, the growth of lithium dendrites during cycling is suppressed, leading to a significant improvement in cycle stability. In addition, Li et al.[111] proposed an integrated comprehensive strategy to construct a highly dispersed BN nanosheet and lithiophilic inorganic components ($Li_2O$ and $Li_2CO_3$) decorated 3D-graphene framework. Due to the Lewis acid and non-conductive nature of BN in the special architecture, lithium metal can be uniformly deposited from top to bottom. They proposed that BN and a large number of inorganic nanoparticles not only generate a uniform electric field to facilitate the migration of $Li^+$; but also contribute to the construction of a strong inorganic-rich SEI with high mechanical and chemical stability.

**3.1.2.3 Additives in separator**

The greatest safety hazard faced by LMBs is the growth of lithium dendrites, which can penetrate the separator and cause internal short circuits and heating, leading to battery combustion or even explosion. Therefore, it is particularly important to improve the separator. Hu et al.[112] improved the thermal conductivity of a commercial separator (Celgard 2325) by directly coating it with BN nanosheets. During cycling, the heat distribution was more uniform, resulting in more uniform lithium plating/stripping and better Coulombic efficiency and cycling performance. Subsequently, their team integrated BN nanosheets into poly (vinylidene fluoride-co-hexafluoropropylene) (PVDF-HFP) using 3D printing technology.[113] The dispersed BN nanosheets not only allow for more uniform heat distribution, but their excellent thermal stability allows the separator to shrink by only 6% after 0.5h of treatment at 150°C. Zhou et al.[114] reported a simple synthetic strategy for large-scale fabrication by coating h-BN/polyimide (PI) onto commercial polypropylene (PP) separators. Due to the presence of h-BN, the separator exhibits good wettability, thermal stability, and thermal conductivity. In addition, the calculation showed that h-BN has weak adsorption on inorganic SEI components, which can induce the formation of a more stable SEI layer, making it both capable of inhibiting lithium dendrites and dendrite blocking.

**3.1.2.4 Additives in liquid electrolyte and gel-polymer electrolyte**

BN nanosheets can be used as additives in both liquid electrolytes polymer electrolytes. Huang et al.[115] reported the use of BN nanosheets as an additive in liquid electrolytes. The BN nanosheets can automatically and continuously flatten the lithium deposition, preventing the formation of lithium dendrites, and reducing the volume changes during the lithium plating/stripping process. The B atoms on BN nanosheets, serving as Lewis acid sites, can interact with Lewis basic anions in the electrolyte, lowering the concentration gradient of $Li^+$ ions and promoting the uniform deposition of lithium.

In the gel polymer electrolyte (GPE), h-BN can play an important role. Lee et al.[116] found that lithium dendrite formation can be suppressed in gel polymer electrolyte (GPE) by incorporating fully fluorinated polyether (PFPE) functionalized 2D h-BN nanosheets (FBN). Even at a low FBN content of 0.5 wt%, the ion conductivity, $Li^+$ transference number, and mechanical modulus of GPE were significantly improved. Using a similar strategy, Reza et al.[117] embedded highly aligned BN nanosheets into a polyvinylidene fluoride composite electrolyte using the direct ink writing (DIW) method. The addition of BN nanosheets resulted in a composite electrolyte with enhanced mechanical strength, electrochemical stability, thermal safety, and a 400% increase in thermal conductivity. Moreover, studies have shown that the binding energy between $TFSI^-$ and BN/PVDF is stronger than that between $Li^+$ and BN/PVDF, which promotes the dissociation of LiTFSI and increases the free migration of $Li^+$.[118] These reports disclose that BN nanosheets can significantly improve the ionic conductivity, $Li^+$ transference number, mechanical modulus, tensile strength, and dendrite suppression ability of the composite polymer electrolyte.

The introduction of BN nanosheets is also beneficial to polyethylene oxide (PEO) based electrolytes. In general, its poor mechanical properties and low ionic conductivity of PEO impede the suppression of lithium dendrite growth. Yao et al.[119] prepared a sandwich-structured BN nanosheets coated PEO polymer electrolyte in which BN serves as a protective layer. The ionic conductivity and mechanical strength of the BN-modified PEO were significantly enhanced. Moreover, the BNNSs-coated PEO polymer electrolyte strongly suppressed lithium dendrite growth. (Figure 6(b1-b6)) Min et al.[120] dispersed BN nanosheets (BNNSs) surface modified with $SiO_2$ in PEO-based electrolyte to prepare PLSB CPE with improved thermal stability and ionic conductivity. Ding et al.[121] also demonstrated that the binding energy of $TFSI^-$ anions to unmodified h-BN was higher than that of $Li^+$. Therefore, the

View Article Online
DOI: 10.1039/D4YA00209A

addition of h-BN can inhibit the diffusion of anions in the composite polymer electrolyte, reducing concentration gradients and polarization, which can improve the stability of lithium deposition. There are similar reports on the positive role of h-BN nanosheets in suppressing the growth of lithium dendrite in PEO electrolytes. [122,123]

**3.1.2.5 Additives in solid-state electrolytes**

As additives in solid-state electrolytes (SSEs), the introduction of h-BN nanosheets can improve the ionic conductivity of SSEs, reduce the thermal runaway of batteries, and suppress the formation of lithium dendrite. One of the constraints limiting the practical usage of SSEs has always been their relatively low ionic conductivity. It is disclosed that the introduction of h-BN can improve the ionic conductivity of SSEs. Choy et al.[124] discovered that the addition of only 1wt% nitride-BN to garnet-type $Li_{6.25}Al_{0.25}La_3Zr_2O_{12}$ (LALZO) SSEs increased the conductivity of the electrolyte by 30 times, surface hardness by 6.6 times, and reduced modulus by 6.3 times. Yang et al.[125] found the reduction of LATP SSEs by lithium metal can be suppressed effectively by using CVD-deposited BN nano-coating on the surface of LATP. It is proposed that the defects in BN can allow lithium ions to pass through, promoting $Li^+$ migration and reducing interface impedance. As an example, Xia et al.[126] constructed a three-dimensional organic/inorganic composite coating by spraying BN-based release agents (BNRA) on the surface of LATP. The BNRA layer not only protected LATP but also formed a Li-N bond in situ, facilitating the migration of Li ions through BN defects at the BNBR/Li interface. Furthermore, the BNRA layer eliminated the risk of thermal runaway by rapid in-plane diffusion.

It is worth mentioning that hybrid solid electrolytes (HSE) have been widely studied for all-solid-state lithium-based batteries due to their high ionic conductivity, mechanical strength, enhanced electrochemical stability, and effective suppression of lithium dendrite growth. Park et al.[127] prepared a standalone hybrid solid electrolyte film using poly(vinylidene fluoride-co-hexafluoropropylene) (PVDF-HFP) as the matrix and $Li_{6.28}Al_{0.24}La_3Zr_2O_{12}$ (LALZO)/ h-BN composite ceramic fillers as the filler. The optimal proportion of h-BN (10 wt%) in the HSE film reduced the crystallinity of the PVDF-HFP matrix, increased the proportion of electroactive β-phase, and improved the mechanical strength of the HSE film, as well as the effective suppression of lithium dendrite growth.

**3.1.3 Alkali-S/O batteries**

**3.1.3.1 The host material of sulfur**

Although the lithium metal anode discussed earlier has great potential, its energy density is still limited by the cathode material when matched with currently used commercial metal oxide positive electrodes. However, the development of L-S batteries has been hindered by issues including the shuttle effect of lithium polysulfides (LiPSs) during charge and discharge, poor electronic conductivity of sulfur cathodes, and large volume change. Therefore, the key scientific problem currently faced by Li-S batteries is to find effective nano-anchoring materials to immobilize soluble LiPSs and suppress their shuttle effect. Through DFT calculations, Jin et al.[128] proposed that the potential of doped and defective BN nanosheets can serve as chemical fixatives for soluble LiPSs species. Dai et al.[129] found that nitrogen vacancies in BN play a critical role in the conversion and fixation of LiPSs, and can enhance the diffusion of lithium ions in the cathode. It is noteworthy that BN nanosheets were frequently used in combination with materials with high conductivity (MXene, [130] Graphene, [131, 132] Graphene Oxide, [132, 134] Carbon nanotube, [135, 136] etc.) to ensure fast electron transfer.

**3.1.3.2 Separator in Li-S batteries**

Many reports proved that the modification of the separator is an effective and straightforward strategy to alleviate the shuttle effect and enhance the electrochemical performance of Li-S batteries.[137] Considering the 2D structure and excellent mechanical properties, it is facile to design or modify the separator using BN nanosheets. Ungyu et al.[138] designed a multifunctional three-layered separator consisting of carbon layers and h-BN layers, which effectively suppresses the shuttle effect of polysulfides. In addition, it effectively protects the lithium metal in the anode from the influence of polysulfides during cycling, enabling stable operation of the anode and exhibiting good cycling retention performance. Through a simple BN nanosheet coating, Chen et al.[139] prepared a multiple-layer separator by coating a thin layer of functional BN (FBN) nanosheets on a commercial Celgard separator. Due to the strong electrostatic interaction between negatively charged polysulfide products and FBN nanosheets, this BN-modified separator can limit the migration of dissolved PSs through the separator, enhance $Li^+$ migration, suppress internal shuttle effect, and enable the cell to have a high capacity, high-rate capability, and long-term cycling stability. Similarly, Xiong et al.[140] prepared a separator composed of P-doped BN and graphene oxide, which provided a synergistic effect of a physical barrier and chemical adsorption for dissolved polysulfides, showing alleviated polarization and promoted kinetic of the cell. Chen et al.[141] reported the introduction of BN in CoB and rGO modified PP separator can effectively restrict the diffusion of polysulfides through enhanced chemical adsorption with $LiS_nLi^+$-N bonding.

Li et al.[142] reported an ultra-thin and highly efficient BN/single-walled carbon nanotube (BN/SWCNT) interlayer (UHEI), which not only hinders the diffusion of polysulfides but also promotes further redox reactions to facilitate the transport of $Li^+$. Additionally, UHEI can significantly improve the electrochemical performance of Li-S batteries under high-sulfur loading (10 mg $cm^{-2}$) and low electrolyte/sulfur (E/S ratio of 8 μL $mg^{-1}$), manifested by higher plateau capacities and lower polarization in discharge.

BN nanosheets can increase mechanical strength greatly. For example, BN modified PVDF separator. can enhance the compressibility of batteries, which can maintain stable cycling for 20 times even when subjected to a pressure of 20 MPa.

**3.1.3.3 Solid-state electrolytes**

The use of SSEs is considered an effective approach to simultaneously addressing the shuttle effect and suppressing lithium dendrite growth. The introduction of BN nanosheets in SSEs can improve the interface compatibility between electrode and electrolyte. Ci et al.[143] prepared a fully solid-state

electrolyte $Li_7P_3S_{11}$ with a small amount of BN nanosheets, in which BN nanosheets can partially isolate $Li_7P_3S_{11}$ solid electrolyte and metallic lithium, thereby improving the interface compatibility between the electrode and electrolyte The solid-state Li-S cells using BN-combined $Li_7P_3S_{11}$ as solid electrolytes exhibited better el good cycling stability and high Coulombic efficiency.

For polymeric-based solid-state electrolytes, BN nanosheet additives can not only enhance the mechanical strength but also improve the ionic conductivity. Zheng et al.[144] developed a BN nanosheets doped polymeric electrolyte (BN-PEO-PVDF) for solid-state lithium batteries. In addition, BN nanosheet additives can promote the thermal response of polymeric electrolytes, leading to faster thermal equilibration and more uniform ion transport in the BN-PEO-PVDF electrolyte.

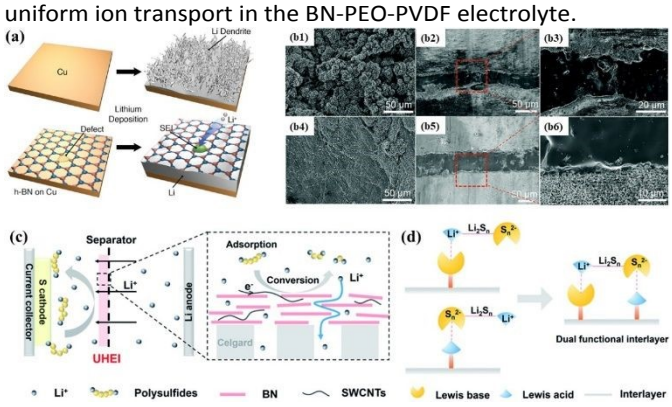


**Figure 6 (a)** Schematic diagrams of lithium deposition and characterizations of h-BN film.[109] Copyright 2014, American Chemical Society. **(b1)** A surface SEM image of the Li electrode from the Li/PEO/Li cell. **(b2 and b3)** Cross-sectional SEM images of the Li/PEO/Li cell. **(b4)** A surface SEM image of the Li electrode from the Li/BNNSs-coated PEO/Li cell. **(b5 and b6)** Cross-sectional SEM images of the Li/BNNSs-coated PEO/Li cell.[119] Copyright 2019, The Royal Society of Chemistry. Schematics showing **(c)** a Li–S battery with a UHEI and **(d)** the advantages of h-BN.[142] Copyright 2022, The Royal Society of Chemistry.

### 3.2 Application of g-$C_3N_4$ in Alkali metal-based Batteries

### Alkali metal ion batteries

#### 3.2.1 Alkali metal ion Batteries

#### 3.2.1.1 Electrode materials additives

Graphitic carbon nitride (g-$C_3N_4$), an organic polymer with a graphene-like structure, has been extensively studied in photocatalysis due to its small band gap, large specific surface area, good chemical stability, low toxicity, and high yield. On one hand, the feasibility of pure g-$C_3N_4$ as anode materials in LIBs was also studied through DFT calculation. Researchers h. Marlies et al.[145] found that when lithium intercalates into the triangular pores of g-$C_3N_4$, the adsorption energy ($E_{ad}$) is as high as −4.2 eV, exceeding the desorption energy of the bulk Li (−3 eV), which makes the adsorbed Li atom difficult to desorb from the structure, resulting in an unstable structure, poor conductivity, and limited reversible capacity. The introduction of defects in g-$C_3N_4$ can improve its electrochemical performance in LIBs[146] to a certain degree. However, g-$C_3N_4$ themselves showed poor electrochemical performance as the anode in LIBs in most cases.

On the other hand, the combination of g-$C_3N_4$, with electrode materials can improve the electrochemical performance because of the N-rich content, and 2D structure. It was later discovered that due to the presence of nitrogen, g-$C_3N_4$ can form hydrogen bonds with anode materials (such as $MoS_2$, $SnS_2$, $Li_4Ti_5O_{12}$, $SnO_2$, Sn, and GO)[147-156] in LIBs, forming a single hybrid material that utilizes the 2D-2D molecular interactions between them.

Shao et al.[157] synthesized $NiCo_2O_4$ directly grown on porous g-$C_3N_4$ nanosheets, where the interconnected $NiCo_2O_4$ nanoparticles can be embedded into the porous nanosheets. Complete coverage of the g-$C_3N_4$ nanosheets minimized the formation of SEI layers, leading to significant synergistic enhancement of both electrochemical activity and stability of the hybrid material. Similarly, Su et al.[158] chose to grow ordered CuO nanorods on 2D Cu/g$C_3N_4$ nanosheets, creating a graded CuO@Cu/g-$C_3N_4$ nanorod film. The resulting film exhibited exceptional stability and cycling performance in both CuO and CuO-based nanoscale architectures, delivering a discharge-specific capacity of 726 $mAhg^{-1}$ after 200 cycles at 0.1C and 457 mAh $g^{-1}$ after 625 cycles at 1C. The presence of porous g-$C_3N_4$ shows the prepared structure with more active sites, facilitating $Li^+$ transport and volume change accommodation. Yao et al.[159] synthesized $MoO_3$@$MoO_2$ heterojunction anchored on two-dimensional g-$C_3N_4$ nanosheets by calcining ammonium molybdate with urea. The two-dimensional porous structure of g-$C_3N_4$ provides abundant active sites for Li-ion storage, enhances its conductivity, and mitigates the volumetric expansion effect during the charge-discharge cycle. In addition, it is reported that g-$C_3N_4$ can buffer the volume change of anode materials. Lin et al.[160] reported a layer-structured g-$C_3N_4$@$WS_2$ composite material synthesized via solvothermal reaction. The synthesized g-$C_3N_4$@$WS_2$ composite material provides abundant reactive sites for lithium storage and sufficient voids to buffer the volume changes of $WS_2$ nanoparticles.

Furthermore, the rich N content in g-$C_3N_4$ can provide more active sites to store lithium. Sun et al.[161] synthesized a laminated g-$C_3N_4$@rGO composite material (g-$C_3N_4$@rGO), (Figure6 (a)) which exhibited excellent cyclic stability (899.3 mAh $g^{-1}$ after 350 cycles at 500 mA $g^{-1}$) and significant rate performance (595.1 mAh $g^{-1}$ after 1000 cycles at 1000 mA $g^{-1}$). The presence of g-$C_3N_4$ in the synthesized g-$C_3N_4$@rGO composite material increased the interlayer spacing of rGO and provided rich n-active sites and microporous structure, thereby greatly improving the Li storage performance. Wen et al.[162] achieved significant performance improvement by uniformly dispersing red phosphorus nanoparticles between the layers of rGO-$C_3N_4$ through a simple high-energy ball milling process. This is attributed to the interface connection formed by P-N and P-C bonding between the red phosphorus and rGO-$C_3N_4$ skeleton, which creates a smooth $Li^+/e^-$ diffusion channel and enhances its mechanical properties. Cui et al.[163] found that the incorporation of g-$C_3N_4$ nanosheets into the $CuCo_2O_4$ nanowire array can not only shorten the diffusion distance of $Li^+$ and the electron transfer pathway but also provide more active sites for $Li^+$ diffusion to the electrolyte, which can buffer the volume expansion and aggregation of $CuCo_2O_4$. Sun et al.[164] found that g-$C_3N_4$ can play a similar effect on $Co_{1-x}S$ anode materials in LIBs. Kim et al.[165] synthesized honeycomb-like Se-doped g-$C_3N_4$ (Se-

H-g-$C_3N_4$) via pyrolysis and selenization, where selenium served as an electron acceptor unit stronger than carbon and nitrogen. Selenium doping also had a significant impact on the electronic structure of the carbon skeleton. This is because Se atoms significantly enlarged the gap between carbon layers, creating more active sites for lithium-ion storage and accelerating the diffusion rate.

Moreover, g-$C_3N_4$ can act as a protective layer on the surface of anode materials. As an example, Pan et al.[166] synthesized a graphene-like carbon nitride/$Mo_2CT_x$ (g-$C_3N_4$/$Mo_2CT_x$) hybrid material by in-situ conversion of urea to g-$C_3N_4$ and achieving the exfoliation of $Mo_2CT_x$ MXene with the construction of a protective layer. Compared to pure $Mo_2CT_x$ (19.2% and 101.4 mAh $g^{-1}$), g-$C_3N_4$/$Mo_2CT_x$ exhibited significantly improved initial Coulombic efficiency (70.8%) and lithium storage performance (525.8 mAh $g^{-1}$). (Figure 7(b))

In SIBs, the incorporation of g-$C_3N_4$ into carbon can enhance the electrochemical performance of SIBs. Taylor et al.[167] obtained stacked multilayered C/g-$C_3N_4$ composites by heating a mixture of inexpensive urea and asphalt in a single pot, which exhibited twice the sodium storage capacity (254 mAh $g^{-1}$) relative to the pristine g-$C_3N_4$ composite. (Figure 7(c)) Similar phenomena were also observed in carbon/g-$C_3N_4$ composites. The high crystallinity of $C_3N_4$, its 2D nanosheet structure with abundant edges and pores as well as the high concentration of pyridinic N are attributed to important factors in enhanced sodium storage.[168] (Figure 7(d1-d6)) Similar to Wu et al.[169] a defective g-$C_3N_4$/graphene heterojunction was prepared by ball milling, and the nitrogen-containing functional groups were controlled to improve the sodium storage capacity.

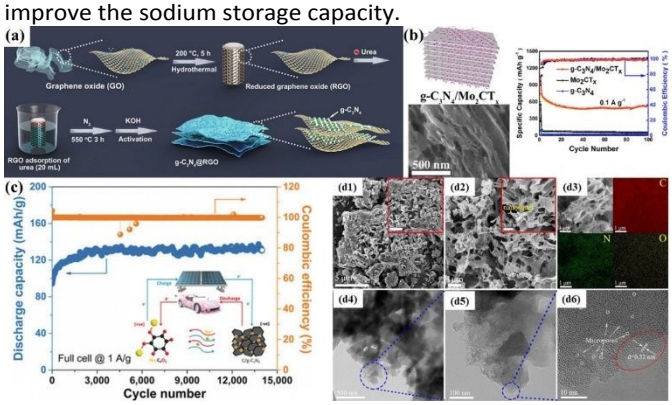


**Figure 7 (a)** Synthesis procedure of g-$C_3N_4$@RGO.[161] Copyright 2018, American Chemical Society. **(b)** Illustrations and SEM images of the prepared g-$C_3N_4$/$Mo_2CT$ structure, along with the cycling stability of the assembled battery at a current density of 0.1 A $g^{-1}$.[166] Copyright 2021, Elsevier. **(c)** Configuration of a C/g-$C_3N_4$ Na full cell consisting of a positive electrode of $Na_2C_6O_6$ and a negative electrode of C/g-$C_3N_4$, and Cycling performance of a C/g-$C_3N_4$ Na full cell at 1 A $g^{-1}$.[167] Copyright 2019, Wiley-VCH. SEM images of **(d1)** PTI and **(d2)** MSGM along with high magnification images inserted in the inset, respectively. **(d3)** EDS elemental mappings and **(d4-d6)** TEM images of MSGM.[168] Copyright 2021, Elsevier.

It has also proved that a combination of g-$C_3N_4$ and conversion-typed anode materials can enhance the electrochemical performance. Avesh et al.[152] reported that g-$C_3N_4$ in ZnS/g-$C_3N_4$ composite can prevent the agglomeration of nanoparticles during the charge/discharge process. The presence of g-$C_3N_4$ alleviated the harmful volume change effect of $Li^+$/$Na^+$ ions during the shuttle in ZnS, leading to the composite anode exhibiting high reversible capacity and initial Coulombic efficiency. Similarly, Im et al.[170] found that the presence of g-$C_3N_4$ can restrain the severe strain caused by volume changes during sodium storage of $SnS_2$.

Furthermore, the presence of g-$C_3N_4$ can enhance the K storage for carbon materials due to the large surface area and more active sites. As an example, Zhang et al.[171] designed and synthesized a one-dimensional/two-dimensional $C_3N_4$/rGO composite material as a host for potassium ions. The resulting composite exhibited a significant specific capacity of 464.9 mAh $g^{-1}$ after 200 cycles at 1 A $g^{-1}$ and 228.6 mAh $g^{-1}$ after 1000 cycles at 10 A $g^{-1}$.

### 3.2.2 Alkali-metal batteries

#### 3.2.2.1 Anode substrate and protective layer

The natural formation of a ring-shaped micro-electric field induced by the six p-electrons of N atoms at the tri-s-triazine units of g-$C_3N_4$ not only gives g-$C_3N_4$ a better lithiophilic, leading to the formation of more Li nucleation sites but also significantly reduces the Li nucleation overpotential. This suggests that g-$C_3N_4$ holds great potential as a promising material for application in LMBs. [172, 173] Due to its lithiophilic and insulation properties, g-$C_3N_4$ can be combined with other conductive materials as both a lithium metal anode substrate and a lithium metal negative electrode protective layer. Yang et al.[174] coated g-$C_3N_4$ on the surface of nickel foam to combine the Lithiophilic of g-$C_3N_4$ with the 3D structure of nickel foam, thereby inhibiting lithium dendrite growth and reducing the volume expansion during the deposition and stripping of lithium metal. (Figure 8 (a)) Hence, the lithium metal anode based on g-$C_3N_4$@Ni foam displayed remarkable electrochemical performances, including high Coulombic efficiency (maintaining 98% after 300 cycles), the ultra-long lifespan of 900 hours, and low overpotential during Li deposition of 1.0 mA h $cm^{-2}$ (<15 mV). Similarly, g-$C_3N_4$-rGO composite with high elasticity and wrinkled structure as a lithium metal anode substrate showed a lower nucleation overpotential and small volume expansion during cycling.[175]

#### 3.2.2.2 Components in artificial SEI layer

Some studies showed that g-$C_3N_4$ can be a good candidate material as a component in the artificial SEI layer because of the rich N-containing functional groups and non-conducting nature. Tu et al.[176] prepared a g-$C_3N_4$ artificial SEI layer with a thickness of only 1 nm on lithium foil. The abundant and uniformly distributed N species in g-$C_3N_4$ can form transient Li-N bonds with lithium ions, thereby regulating the flux of lithium ions and enabling stable plating/stripping processes. Kang et al.[177] designed a uniform and dense artificial interface by wrapping carbon nanofibers in commercial carbon cloth using g-$C_3N_4$ coating to wrap, Lithium metal can selectively deposit into the interlayer between g-$C_3N_4$ and CC, where g-$C_3N_4$ as an artificial interphase has favorable lithiophilic properties, capable of regulating the distribution of Li ions and eliminating dendritic hotspots. Thus, uniform lithium deposition can be achieved for this substrate, leading to a large-capacity metal Li storage. (Figure 8(b1-b3)) Furthermore, it is beneficial to coat g-$C_3N_4$ on the surface of MXene [178] and LiMg-LiH[179] as artificial SEI to improve the performance of LMBs.

It is also effective to coat g-$C_3N_4$ on the lithium metal to enhance the electrochemical performance in LMBs. [180]

### 3.2.2.3 Separator additives

Differing from previous reports on artificial protective layers, Kim et al.[181] constructed a dual lithiophilic interlayer on the separator surface, which, although coated onto the separator, effectively functions similarly to an artificial SEI layer due to its direct contact with the lithium metal. The dual lithiophilic interlayer constructed exhibits affinity for both $Li^+$ and $Li^0$, featuring enhanced Lewis basicity and orbital hybridization concepts. Furthermore, the strong interaction between $Li^+$ and the dual lithiophilic interlayer facilitates the charge transfer process. Under the driving force of orbital hybridization, the deposition of the lithium metal layer beneath the dual lithiophilic interlayer occurs in a planar growth mode, alleviating electrolyte decomposition. (Figure 8(c)) The Li/Li symmetric cells employing the dual lithiophilic interlayer exhibited over 400 cycles at 2 mA $cm^{-2}$ and 2 mAh $cm^{-2}$.

**3.2.2.4 Additives in Electrolyte and Gel-polymer Electrolyte**

As an additive in polymer electrolytes, g-$C_3N_4$ can play a unique role in improving the electrochemical performance of electrolytes. Li et al.[182] utilized g-$C_3N_4$ as an additive to mix with [bis(trifluoromethanesulfonimide) lithium salt/di(ethylene glycol) dimethyl ether] (LiTFSI-DGM), creating a slurry-like polymeric electrolyte. Benefiting from the advantages of high mechanical strength and layered structure availability, g-$C_3N_4$ effectively inhibits lithium dendrite growth. This slurry-like electrolyte exhibits reduced anode-electrolyte interface resistance (115 Ω·$cm^2$) and decreased Li plating/stripping overpotentials (reaching as low as 50 mV and 100 mV, respectively, at 0.5 mA $cm^{-2}$ and 2 mA $cm^{-2}$). Zhang et al.[183] introduced g-$C_3N_4$ nanosheets into the PVdF-HFP based solid polymer electrolyte (SPE). This effectively disrupted the ordered arrangement of polymer segments in solid-phase extraction, reducing the crystallinity of the solid electrolyte and facilitating faster migration of lithium ions within the PVDF-HFP matrix. Moreover, the pyridinic N on the g-$C_3N_4$ nanosheets can be considered as a Lewis base, promoting the dissociation of LiTFSI and increasing the concentration of free lithium ions. In addition, the presence of 2D g-$C_3N_4$ can improve the mechanical strength, reduce the crystallinity, suppress the lithium dendrite formation,[184]and enhance the thermal stability in PVDF-HFP based electrolytes. [185]

The addition of g-$C_3N_4$ in the PEO electrolyte can significantly enhance its cycling stability towards lithium anodes as g-$C_3N_4$ widens the electrochemical window of the electrolyte, preventing direct contact between PEO and lithium. [186] The presence of electronegative N species in g-$C_3N_4$ ensures the uniform deposition of lithium ions. Because g-$C_3N_4$ has abundant Lewis basic active sites, the addition of g-$C_3N_4$ in PEO-based electrolyte can regulate the distribution of $Li^+$ ions, hereby inhibiting the growth of lithium dendrites.[187] Symmetrical cells assembled with this CSE successfully cycled for 1400 hours at 0.1 mA $cm^{-2}$ and 60°C. Additionally, PCN reduces the crystallinity of PEO and promotes the dissociation of LiTFSI, effectively enhancing the $Li^+$ conductivity of the electrolyte (3.47 × $10^{-4}$ S $cm^{-1}$ at 60°C).

Besides the enhancement of mechanical strength and thermal stability, the presence of uniformly distributed g-$C_3N_4$ nano-fillers can significantly reduce the crystallinity of the polymer electrolyte and promote $Na^+$ dissociation through the interaction between surface N atoms and sodium salts, resulting in a better performance.

**3.2.2.5 Solid-state electrolyte**

The addition of g-$C_3N_4$ nanosheets into solid-state electrolytes can change the contact between lithium metal and SSEs. Huang et al.[188] demonstrated that the addition of g-$C_3N_4$ nanosheets into molten lithium can transform the point contact between lithium metal and the garnet-type solid electrolyte into intimate contact. Additionally, the increased viscosity of the molten lithium reduces its surface tension, significantly enhancing the energy to suppress lithium dendrite growth.

As a 2D nanosheet, g-$C_3N_4$ can be assembled in the interlayer of inorganic solid electrolyte. Wang et al.[189] fabricated a layered inorganic solid electrolyte (LLZO/CN LISE) with a thickness of 30 μm by assembling LLZO nanosheets into a layered framework and growing g-$C_3N_4$ in situ at the interlayer spacing. At 25°C, the LLZO/CN LISE exhibited an ion conductivity of 2.50 × $10^{-4}$ S $cm^{-1}$, providing a high ion conductivity of 167 mS. Moreover, g-$C_3N_4$ formed tight bonding with adjacent LLZO layers, resulting in excellent mechanical properties of the LLZO/CN LISE.

**3.2.3 Additives in Alkali-S/O battery**

**3.2.3.1 The host of sulfur**

Because of the rich N content and high polarity of g-$C_3N_4$, g-$C_3N_4$ exhibits superior chemical adsorption capability for LiPSs, effectively suppressing their dissolution in the electrolyte. The earliest application in 2016, Pang et al. utilized graphitic carbon nitride ($C_3N_4$) as an efficient sulfur-based matrix to enhance the cycling stability of lithium-batteries.[190, 191] The pyridinic nitrogen-rich structure in g-$C_3N_4$ exhibits superior chemical adsorption capability for LiPSs. According to DFT calculations, [192] The results indicate that g-$C_3N_4$ is favorable for achieving anchoring effects toward LPSs through both chemical bonding and physical confinement of the relevant species. g-$C_3N_4$ provides an appropriate binding energy, enhancing the redox kinetics. Dispersion interactions are mainly concentrated near sulfur atoms, and the bonding and charge transfer between Li-N/C-S result in a strong anchoring effect. Additionally, the strong coupling interactions formed by g-$C_3N_4$ can alleviate the interaction between LPSs and solvents, thereby playing a dissolution-mitigating role.

Although feasible in the theoretical calculation, however, the limited conductivity of g-$C_3N_4$ itself hampers its practical application. The composites of BN-based composites can overcome the disadvantage of g-$C_3N_4$. Kuang et al.[193] fabricated a 3D lightweight and porous $C_3N_4$ nanosheets @ rGO (g-$C_3N_4$@rGO) network as a sulfur host. The PCN incorporated in the nanocomposite provides high nitrogen content (18.99%) for chemically anchoring lithium polysulfides, while the rGO in the nanocomposite facilitates rapid electron transfer. Furthermore, the high surface area of the 3D network provides open channels for ion diffusion and electrolyte accessibility. A similar

strategy[194, 195](Figure 8(d1-d6)) shows an example of rGO/g-$C_3N_4$/CNT as a host of LiPSs. Besides the chemical adsorption of rGO and CNT, the enriched nitrogen (N) atoms in g-$C_3N_4$ exhibit strong chemical adhesion for LiPSs anchoring. The dual immobilization mechanism effectively alleviates the "shuttle effect" in Li-S batteries. The discharge capacity of the rGO/g-$C_3N_4$/CNT/S cathode after 500 cycles is 620 mAh $g^{-1}$, with a low capacity decay rate of only 0.03% at 1C. The elevated nitrogen content in g-$C_3N_4$ effectively enhances the cycling stability of Li-S batteries and their chemical interactions with polysulfides. [196]

Furthermore, due to the significantly increased number of active sites facilitated by the high specific surface area of g-$C_3N_4$, its combination with materials such as graphene, [197] carbon hybrid cages,[198] carbon nanotubes (CNT),[199, 200] TixOy-$Ti_3C_3$, [201] rGO (Polypyrrole coated g-$C_3N_4$),[202] carbon cloth,[203] $MoSe_2$,[204] MXene[205] and Ni[206] as S hosts has exhibited excellent suppression of polysulfide shuttle effects. In particular, Chen et al.[207] synthesized a composite of ultrathin $MoS_2$ nanosheets and nitrogen-enriched g-$C_3N_4$. The strong chemical interactions between $MoS_2$ and nitrogen-rich g-$C_3N_4$ with lithium polysulfides effectively hinder the shuttle effect in Li-S batteries, resulting in stable cycling performance and outstanding rate capability, while also efficiently suppressing self-discharge behavior.

In addition to composites with other materials, Huang et al.[208] utilized heterojunctions formed between two precursors of g-$C_3N_4$ to effectively tune the electronic cloud structure and interface adhesion energy of g-$C_3N_4$. This close g-$C_3N_4$/g-$C_3N_4$ interface imparts significantly accelerated reaction kinetics and enhanced ion and electron transport.

**3.2.3.2 Separator additives**

The coating of g-$C_3N_4$ on the surface of the separator is also effective in trapping and fixing polysulfides. Wang et al.[209] coated commercial separator surfaces with transition metal coordinated g-$C_3N_4$ and crystalline carbon (M-$C_3N_4$/C). This coating exhibits excellent trapping ability and rapid conversion capability for polysulfides. The uniformly distributed transition metals on g-$C_3N_4$/C serve as active centers to regulate the behavior of polysulfides, displaying strong chemical adsorption capacity and high catalytic activity towards polysulfide conversion. When combined with other functional materials, the capability of trapping polysulfides for g-$C_3N_4$ can be further improved. Wang et al.[210] designed a novel dual-functional separator, where a self-assembled FeOOH layer was firmly formed on the PP separator surface to chemically capture soluble polysulfides and prevent shuttle effects. Subsequently, a coated g-$C_3N_4$/KB layer was introduced to greatly enhance the migration of lithium ions and physically confine the migration of intermediate products. As a result, batteries employing this dual-functional separator (referred to as G-SFO) achieved remarkable rate capacities (1000, 901, and 802 mA h $g^{-1}$ at 0.5, 1, and 2 C, respectively).

The doping to g-$C_3N_4$ can further improve the trapping capability, as illustrated by Co-doped g-$C_3N_4$, [211] in which doped heteroatoms can play a role in catalytic conversion, effectively mitigating shuttle effects.

**3.2.3.3 The catalysts of Li-O battery**

Thanks to its high nitrogen content, g-$C_3N_4$ facilitates a simple synthesis process and possesses more active reaction sites compared to other nitrogen-doped carbon materials, making it considered a viable non-metallic electrocatalyst for oxygen reduction reaction (ORR). Liu et al.[212] reported a non-metallic, standalone mesoporous graphene@graphitic carbon nitride (g-$C_3N_4$) composite air cathode material. In this material, g-$C_3N_4$ nanosheets function as efficient electrocatalysts, while mesoporous graphene nanosheets provide spatial accommodation for $Li_2O_2$ deposition and promote electron transfer. The results demonstrate that compared to a pure graphene air electrode, the graphene@g-$C_3N_4$ composite air electrode exhibits a lower charging plateau by 0.48 V, a higher discharging plateau by 0.13 V, and a discharge capacity approaching 17300 mA h $g^{-1}$.

Moreover, the conductivity and catalytic activity of g-$C_3N_4$ can be enhanced by incorporating it with other materials that possess better conductivity. For instance, the combination of g-$C_3N_4$ with Co,[213] Fe,[214] and Ni-$Co_3O_4$,[215] among others, non-precious metal composites, has been investigated as effective catalysts in fuel cells and LOBs. These composite materials exhibit excellent ORR (oxygen reduction reaction) and OER (oxygen evolution reaction) activity and durability, comparable to commercial Pt/C catalysts. Shui et al.[216] utilized a low-cost non-precious metal composite of $LaNiO_3$ and g-$C_3N_4$ as a dual-functional electrocatalyst for the air electrode in lithium-oxygen batteries. The compositional strategy altered the electronic structure of $LaNiO_3$ and g-$C_3N_4$, ensuring a higher $Ni^{3+}/Ni^{2+}$ ratio and increased hydroxyl surface adsorption on CNL, thereby promoting the oxygen reduction reaction (ORR) and oxygen evolution reaction (OER). Yu et al.[217] synthesized a composite material of $CoFe_2O_4$/g-$C_3N_4$, where the layered structure of g-$C_3N_4$ facilitated the transport of oxygen and lithium ions and hindered the aggregation of $CoFe_2O_4$ particles. During the charge-discharge reactions, the $CoFe_2O_4$ material accelerated the decomposition of $Li_2O_2$, thereby reducing electrode polarization.

In addition, single-atom metal catalysts have been demonstrated to decrease costs and more effectively utilize precious metals. Building upon this, Qian et al.[218] synthesized single-atom Pt catalysts (Pt-CNHS) supported on hollow ultrathin g-$C_3N_4$ nanosheets through a liquid-phase reaction between g-$C_3N_4$ and $H_2PtCl_6$. The single-atom Pt catalyst exhibits electrochemical activity. Based on experimental results and DFT calculations, the excellent electrocatalytic activity of Pt-CNHS can be attributed to its large specific surface area, enhanced conductivity, efficient interfacial mass transfer between Pt atoms, and porous structure.

Inspired by the excellent performance of g-$C_3N_4$ in photocatalysis, Zhang et al.[219] designed a novel photo-responsive cathode by in-situ growth of Co-doped $C_3N_4$ (Co-$C_3N_4$) on carbon paper (CP). The Co doping not only enhanced the conductivity and electrocatalytic ability of $C_3N_4$ but also facilitated bandgap tuning, broadening the wavelength range of light response, and enhancing the photocatalytic performance of $C_3N_4$. Anik et al.[220] utilized g-$C_3N_4$/rGO nanocomposites as photocatalysts for efficient light-assisted charging in lithium-

oxygen batteries. The formation of new C-C bonds between g-$C_3N_4$ and rGO during the decomposition process of melamine led to a red shift in the absorption edge of the nanocomposites. This red shift resulted in a reduction of the optical band gap of the nanocomposites, enhancing the capture and utilization of visible light. By employing the nanocomposites as photoelectrodes in lithium-oxygen batteries, a significant reduction in charging potential, particularly at high current densities, was achieved, leading to improved cycling performance of the batteries.

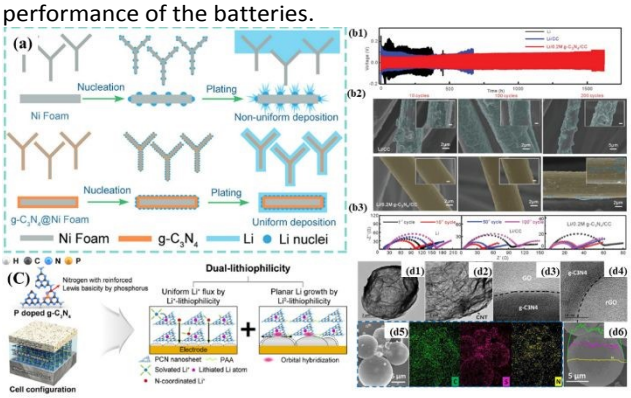


**Figure 8 (a)** Schematic of the Li nucleation and plating process on Ni foam and g-$C_3N_4$@Ni foam.[174] Copyright 2019, Wiley-VCH. **(b1)** The voltage profiles of Li–Li symmetric batteries with bare Li, Li/CC, and Li/0.2 mg-$C_3N_4$/CC electrode at a current density of 2.0 mA $cm^{-}2$. **(b2)** The SEM images of Li/CC and Li/0.2 m g-$C_3N_4$/CC after 10, 50, and 100 cycles in Li–Li symmetric batteries. **(b3)** The Nyquist plot of impedance spectra of Li–Li symmetric batteries with Li/CC and Li/0.2 m g-$C_3N_4$/CC electrode after different cycles.[177] Copyright 2019, Wiley-VCH. **(c)** Schematic illustration for the lithium deposition mechanism under dual-lithiophilic interfacial layer.[181] Copyright 2022, Elsevier. **(d1, d2)** High-resolution TEM (HRTEM) images of GO/g-$C_3N_4$/CNT **(d3)** and rGO/g-$C_3N_4$/CNT **(d4)**. **(d5)** SEM image and EDS elemental mapping of rGO/g-$C_3N_4$/CNT/S. **(d6)** Elemental line scan of rGO/g- $C_3N_4$/CNT/S.[195] Copyright 2019, American Chemical Society.

### 3.3 Application of MMT and VMT in Alkali-based Batteries

#### 3.3.1 Alkali metal ion Batteries

##### 3.3.1.1 Electrode material additives

Montmorillonite (MMT) is a naturally abundant and cost-effective clay mineral consisting of two layers of silica tetrahedra and aluminum octahedra sandwiched between them. Intercalation of hydrated cations occurs between the layers to balance the charge through van der Waals forces. MMT possesses a high surface area, cation intercalation/exchange capacity, scalability, and excellent thermal/hydrothermal stability making it highly promising for applications such as adsorbents, catalysts, sensors, and filtration membranes.

In the field of energy storage, MMT nanosheets themselves are not suitable to act as anode materials due to their non-conductive nature although there have been several reports on this. [221, 222] However, MMT can be employed as an auxiliary material in combination with other anode materials to enhance the electrochemical behavior. Shen et al.[223] disclosed that the addition of MMT nanosheets can enhance the structural stability and reversibility of hard carbon materials, as shown in Figure 9(a,b).

The incorporation of MMT facilitates the formation of a mechanically stable SEI layer, reducing the electrolyte decomposition and maintaining the integrity of the electrode structure. Yang et al.[88] utilized MMT to construct a novel electrode/electrolyte interface for lithium-graphite dual-ion batteries (DIBs). The prepared SEI film can modulate the anion intercalation/deintercalation behavior, facilitating the rapid migration of anions while preserving the graphite structure from degradation. MMT may react with the electrolyte decomposition products, such as HF, potentially avoiding the corrosion of battery components under high voltage conditions.

##### 3.3.1.2 Separator additives

MMT as additives

Due to the high porosity and thermal stability of MMT, it finds extensive applications in the field of separators. Lanceros-Mendez et al.[224] prepared MMT/P(VDF-TrFE) porous films with varying MMT contents using a solvent-casting method for LIBs. The encapsulation of MMT increased the average pore size, porosity, and electrolyte solution absorption of the film. The addition of fillers enhanced the mechanical properties of the film. The presence of clay slightly improved the ionic conductivity, while significantly improving the temperature stability. MMT nanosheets can be an efficient additive to enhance the thermal stability, mechanical strength, and ionic conductivity of polymer-based separators due to their inorganic components and 2D structure. [225, 226, 227] (Figure 9(c))

**VMT as additives**

Due to the high stability of sepiolite at temperatures above 1000 °C, Pol et al.[228] chose to coat one side of polypropylene with a 7 μm layer of 1:9 sepiolite to PVDF to enhance the thermal stability of the separator. Calorimetry experiments showed that the sepiolite-PVDF modified PP had a lower heat release rate (101.7 J $g^{-1}$ for PP, 83.16 J $g^{-1}$ for the modified separator) and a slightly higher melting point (ΔT = +3.38°C). This demonstrates that the sepiolite modified separator improves safety. Further research on increasing the amount of sepiolite will result in separators with even higher melting points. Zhang et al.[229] incorporated sepiolite nanoparticles (VMT) and laponite nanoparticles (LPT) into a polyvinylidene fluoride (PVDF) matrix to prepare organic-inorganic composite membranes for LIBs. (Figure 9(d)) The membrane exhibited the best performance when the ratio of the two inorganic nanoparticles was 1:1. The prepared separator demonstrated the highest ionic conductivity (0.72 mS $cm^{-1}$) and the lowest interfacial impedance (283 Ω) at room temperature. Furthermore, the addition of VMT and LPT nanoparticles effectively reduced the thermal shrinkage of the membrane, improved the thermal dimensional stability, electrolyte uptake, and porosity of the membrane. Tu et al.[230] discovered that the addition of two-dimensional sepiolite nanosheets greatly improved the thermodynamic instability of PVDF/N, N-dimethylacetamide (DMAc) solution, leading to the formation of elongated finger-like porous structures. When the content of the sepiolite nanosheets (VNs) was 7.0 wt%, the ion conductivity of the separator increased from 0.300 mS $cm^{-1}$ to 1.679 mS $cm^{-1}$, and the thin film exhibited good thermal stability, with a 2.3°C increase in melting point compared to neat PVDF. The tensile strength and Young's modulus significantly increased by 168% and 172%, respectively.

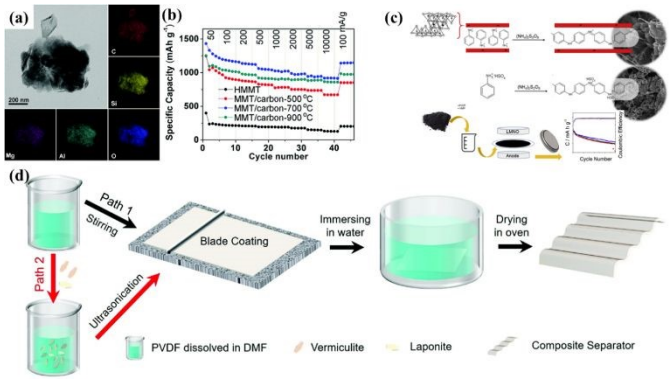


**Figure 9 (a)** TEM image and element mapping of MMT/carbon-700 °C. **(b)** Rate performance at a range of current densities from 50 to 10000 mA $g^{-1}$.[223] Copyright 2020, The Royal Society of Chemistry. **(c)**The polymerization of anilinium in the interlamellar space of MMT form an intercalated nanocomposite where the emeraldine positive charges are balanced with the negative charges of MMT. [227] Copyright 2021, Elsevier. **(d)** Schematic illustration of the preparation of composite separators.[229] Copyright 2022, The Royal Society of Chemistry.

#### 3.3.1.3 Additives in Electrolyte and Gel-polymer Electrolyte

Due to the 2D nanosheet structure, alkylammonium ion spacing/coupling agents and PVDF-HFP copolymers can be intercalated in the planar layers of MMT. [231] The prepared solid polymer electrolytes (SPEs) demonstrate good ion conductivity (e.g., $10^{-6}$ S $cm^{-1}$), solvent retention capabilities, and dimensional stability. Subsequently, Park et al. [232, 233] separately introduced lithium-ion and organically modified MMT into PEO-based electrolytes. The addition of MMT in both cases significantly enhanced the ion conductivity of the electrolyte and effectively reduced the crystallinity of the polymer.

Due to the unique $Li^+$. . . O-Si interactions present in the nano-OMMT, the transfer of $Li^+$ ions within the plastic polymer electrolyte occurs more easily. As a result, a higher ion conductivity of $1.67 \times 10^{-14}$ S $cm^{-1}$ and a migration number of 0.67 were achieved. Similar reports were also reported by Cheng et al. [235] about a novel functionalized poly(meta-phenylene isophthalamide) (PMIA)/MMT based gel polymer electrolyte (GPE) using electrospinning technique. Well-dispersed MMT fillers within the PMIA membrane can provide an electro-negative atmosphere, facilitating the convenient transport of lithium ions across the separator.

### 3.3.2 Alkali-metal batteries

#### 3.3.2.1 Anode substrate

Thanks to the lithiophilic nature of MMT, it holds great potential as a lithium metal anode substrate. Zhu et al.[236] employed MMT-coated copper foil as a robust substrate to promote uniform and stable Li nucleation. The results show that, at 2 mA $cm^{-2}$ and an aerial capacity of 1 mAh $cm^{-2}$, a Coulombic efficiency as high as 99% was achieved after 700 cycles. Due to the similar properties such as high electronegativity shared between VMT and MMT, they can effectively adsorb $Li^+$ and facilitate the deposition of $Li^+$. Luo et al.[237] proposed the use of a soft-hard organic-inorganic layered pearl structure to suppress lithium dendrites. In this structure, lithium metal is employed as the soft component, while VMT particles serve as the hard inorganic component, exhibiting a theoretical modulus 30 times higher. VMT flakes possess a high negative charge. They can absorb a large number of lithium ions in the electrolyte and then co-deposit with lithium ions, effectively suppressing the growth of lithium dendrites and forming a branch-free rock-like structure after hundreds of cycles. After the deposition of surface-adsorbed $Li^+$, the VMT flakes regain their negative charge and move away from the substrate along the electric field, facilitating the further absorption of new $Li^+$ ions and enabling uniform deposition in a shuttle-like manner. (Figure 10(a)(b))

#### 3.3.2.2 Artificial SEI layer components

The interlayer spacing of MMT provides a fast pathway for $Li^+$ transport and its inherent lithiophilicity makes it a promising candidate for artificial SEI layer on lithium metal anodes. Li et al.[238] enhanced the SEI performance and suppressed the growth of dendritic crystals by utilizing Li-ion modified MMT (Li-MMT), resulting in significant improvements in electrochemical performance. The Li-MMT SEI not only possesses inherent fast $Li^+$ channels but also serves as a reservoir, providing sufficient lithium ions between and at the edges of Li-MMT nanoplates for rapid interlayer and intralayer transfer of lithium ions. Furthermore, Shu et al.[239] employed a similar strategy using Li-MMT as an artificial SEI layer, and their research primarily demonstrated that Li-MMT can serve as a single pathway for lithium ions, inhibiting the transport of $TFSI^-$ anions within the MMT layer and alleviating the concentration gradient of $Li^+$ at the interface.(Figure 10(c)(d)) Zhang et al.[240] proposed the use of an Ag-montmorillonite (AMMT) interlayer $Li^+$ conductor as an interface ion transport precision flow pump to induce rapid and reversible electrodeposition/stripping of Li metal. The negatively charged layer and inherent channels of the AMMT pump can reduce the nucleation barrier and facilitate $Li^+$ transport.

VMT nanosheets-based organic-inorganic hybrid film showed a similar effect in suppressing dendritic growth and mitigating volume fluctuations.[241] The improved reason is related to the mechanical strength of the VN layer.

#### 3.3.2.3 Separator additives

The 2D inorganic non-conductive materials can be used as additives to improve the performance of separators in batteries. He et al. incorporated clay with atomic interlayer ion channels into a polymer separator using electrophoretic deposition technique.[242] Due to the strong adsorption energy between Li-MMT and PVDF-HFP, the Li-MMT/PVDF-HFP membrane exhibits significantly improved electrolyte wettability, thermal stability, mechanical strength, and electrochemical performance. The parallel ion channels with unified $Li^+$ flow direction lead to uniform deposition of lithium ions, resulting in dendrite-free lithium anodes. Wang et al. coated lithium-modified MMT (Li-MMT) onto a porous PP membrane.[243] The Li-MMT facilitated a unified flow direction of lithium ions, resulting in the uniform deposition of lithium ions on the anode surface and suppression of lithium dendrite formation. A similar enhancement for MMT nanosheets as an additive can be found in PVDF/PAN/VMT [244] and PP/VMT[245] in polymer separators.

#### 3.3.2.4 Additives in Electrolyte and Gel-polymer Electrolyte

In addition, MMT can also function as an additive in liquid electrolytes. Yan et al. [246] introduced MMT as a nucleophilic medium into the host electrolyte to modulate the ion distribution of lithium dendrite deposition. The redistribution of lithium ions effectively suppresses the formation of ion-depleted zones on the anode surface by increasing the ion concentration at the electrode/electrolyte interface, further delaying the occurrence of dendritic growth. As the deposition process proceeds, MMT serves as heterogeneous nucleating seeds for Li ion adsorption, promoting uniform deposition instead of large clusters or lithium dendrites.

MMT can be used as a functional additive in quasi solid-state electrolyte. For example, Park et al.[247] designed a UV-crosslinked nanocomposite polymer-clay solid electrolyte (U-CPCE). The addition of MMT not only altered the local crystallinity of the polymer matrix, increasing the amorphous region for ion conduction, but also intervened in the ion-ion and ion-polymer interactions, enhancing the carrier concentration. It plays a crucial role in improving ion conductivity and facilitating $Li^+$ migration, thus enabling excellent electrochemical battery performance. Ding et al.[248] designed and fabricated a novel composite solid electrolyte (CMP/MMT), composed of a robust interpenetrating polymer network matrix and layered MMT flakes. The ion transport pathways are well connected, allowing full access of the active materials. The addition of MMT not only enhances the room temperature ionic conductivity and $Li^+$ migration number but also provides mechanical support to the soft polymer network, effectively preventing short circuits under mechanical deformation, thereby exhibiting excellent electrochemical performance. Salot et al.[249] incorporated MMT as an inorganic filler into a PVDF-HFP-based gel electrolyte, resulting in an electrolyte with high ion conductivity (0.48 mS $cm^{-1}$ at 25°C) and excellent thermal stability up to 140 °C.

VMT nanosheets can work as additives in polymer based electrolyte. He et al.[250] prepared VMT nanosheets (VNs) with abundant cation vacancies and incorporated them into a PEO/PVdF-HFP blend polymer electrolyte. The cation vacancies not only provided additional Lewis acid-base interaction sites for lithium ions but also protected the PEO chains from excessive lithium ion oxidation, thereby enhancing the dissociation of lithium salt and the hopping mechanism of lithium ions. Luo et al.[251] investigated vertically aligned two-dimensional VMT nanosheets (VAVS) as advanced fillers for solid polymer electrolytes (SPE), exhibiting enhanced ion conductivity, $Li^+$ transference number, mechanical modulus, and electrochemical stability. Jiang et al.[252] investigated a layered ionic liquid composite electrolyte (L-ILCE) by encapsulating the ionic liquid (ILs) within the ordered interlayer nanochannels of a VMT framework. Within the nanochannels, the fine microstructure induces the rearrangement and crystallinity of the ionic crystals, endowing L-ILCE with the combined advantages of liquid electrolytes and solid electrolytes. L-ILCE exhibits high ion conductivity (0.09-1.35 × $10^{-3}$ S $cm^{-1}$ over −40 to 100 °C) while polymers and inorganic electrolytes typically lose their ion conductivity below 0 °C.

#### 3.3.4 Alkali-S batteries

The interaction between 2D MMT nanosheets and polysulfides can restrain the shuttle effect of polysulfides because Si-OH groups as Lewis acid sites can form bonds with polysulfides, which effectively inhibits the diffusion of polysulfides to the anode. [253] Furthermore, benefiting from the interlayer cation exchangeability of MMT, the following researchers have developed various ion-intercalated MMTs to change the charge of MMT. Thus, carbon-intercalated MMT (MMT@C),[90] Li-MMT,[243, 254-256] and $FeS_2$ intercalated MMT ($FeS_2$@MMT),[91] etc were developed. Among them, Li-MMT is more widely applied due to the presence of lithium ions in its interlayers, which facilitates faster $Li^+$ transport within the material. Zhang et al.[257] utilized naturally occurring minerals with 1D to 3D microstructures as advanced separators for Li-S batteries. The cell using MMT/CB-Celgard separator exhibited the highest upper plateau discharge capacity (369 mA h $g^{-1}$), initial reversible capacity (1496 mA h $g^{-1}$ at 0.1 C), rate performance, and cycling stability (666 mA h $g^{-1}$ after 500 cycles at 1.0 C with a capacity decay of 0.046% per cycle). Even with a high sulfur loading (8.3 mg $cm^{-2}$), the MMT/CB-Celgard separator demonstrated stable cycling in Li-S batteries. (Figure 10(e)).

Additionally, MMT is often used in conjunction with other materials possessing different properties. Li et al.[258] developed a multifunctional material composed of MMT and selenium-doped sulfur-polyacrylonitrile ($Se_{0.06}$SPAN) support. MMT provides sufficient channels for $Li^+$ transport, while selenium-doped sulfur-polyacrylonitrile catalyzes the conversion of "dead sulfur" and contributes to the overall capacity.

MMT nanosheets have a better ionic conductivity, thus MMT nanosheets can be combined with materials with high electronic conductivity to provide a fast ion/ electron transport. As an example, Shao et al.[255] have designed a two-dimensional (2D) heterostructure by integrating monolayer lithium-montmorillonite (MMT) with nitrogen-doped rGO. The low diffusion barrier layer on Li-MMT facilitates rapid $Li^+$ transport, while the adjacent RGO constructs a highly conductive electron network, enabling efficient adsorption-diffusion-conversion of polysulfides and achieving fast electrochemical reaction kinetics.

The addition of VMT in the electrode can act as a host for sulfur loading to confine elemental sulfur and immobilize polysulfides, resulting in enhanced rate and cycling performance. [259] Compared to conventional carbon-sulfur composite materials, VMT-sulfur composites demonstrate improved rate performance and enhanced cycling stability. (Figure 10(f))

**VMT in Li-S batteries**

VMT-based separators can inhibit the diffusion of polysulfides on the separator through electrostatic interactions and spatial hindrance. [260] Meanwhile, the inorganic thin flakes with high strength and Young's modulus can prevent the penetration of metallic lithium dendrites, resulting in improved safety of the battery. Wang et al.[261] prepared a thin film composite solid electrolyte (LCSE), namely Vr/PEO-LCSE, by filtering VMT nanosheets and subsequently embedding PEO-LiTFSI into the interlayer via an expansion filtration method. The continuous interlayer channels exhibit favorable PEO chain mobility and

View Article Online
DOI: 10.1039/D4YA00309A

LiTFSI dissociation, resulting in an ion conductivity of $1.22\times10^{-5}$ S $cm^{-1}$ at 25 °C for Vr/PEO-LCSE.

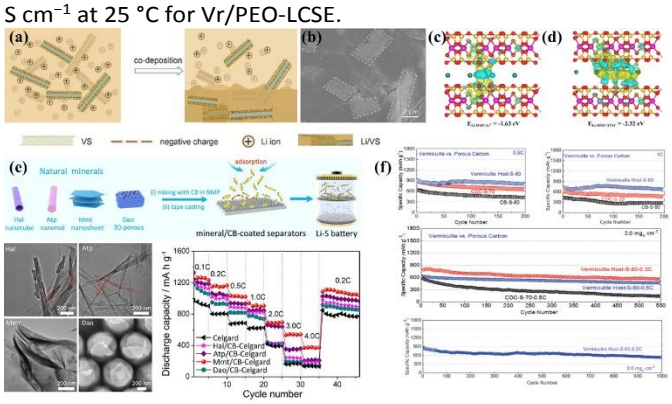


**Figure 10 (a)** Schematic illustrating the co-deposition of Li with VS. **(b)** BSE image of Li plating in EC/DEC electrolyte with 0.1% VS.[237] Copyright 2023, Nonferrous Metals Society of China. The differential charge densities of **(c)** Li-MMT with $TFSI^-$ ions (Li-MMT–TFSI) and **(d)** Li-MMT with $Li^+$ ions (Li-MMT–$Li^+$) and the corresponding adsorption energies.[240] Copyright 2021, Wiley-VCH. **(e)** Schematic illustration of preparation of the mineral/CB-coated separators, transmission electron microscopic (TEM) images of Hal, Atp, Mmt, Dao. And rate performance of the Li-S batteries with different separators and the CNT/S cathode.[257] Copyright 2021, Elsevier. **(f)** Comparison studies of cycling performance and long-term cycle stability of the VMT–Sulfur cathodes with different S contents at the mass loading of 2.0 mg $cm^{-2}$.[259] Copyright 2022, Wiley-VCH.

Table 1 and 2 summarized the application of 2D inorganic non-conductive materials in alkali metal based batteries. In all, these materials can be used as additives of SEI building block, separators and electrode substrate to improve the electrochemical performance of alkali metal based batteries.

## 3.4 Challenges and outlook

The application of 2D inorganic non-conductive materials in enhancing the performance of alkali metal based batteries has achieved certain successes, but there are still many challenges that need to be carefully considered.[262] First, methods for producing high-quality 2D materials on a large scale with a low cost are still lacking at present time. For example, it is reported that the industrial-scale efficiency to prepare BN nanosheets using exfoliation of BN bulk material is much less than 30%.[263] Moreover, many 2D inorganic nanosheets are prepared by exfoliation of the corresponding bulk layered materials. Thus, defects and/or impurities can be introduced to 2D inorganic materials during preparation process. Thus, it is highly desirable to develop novel method to prepare inorganic nanosheets with a large scale.[264] Secondly; it remains a big challenge to synthesize the 2D inorganic materials with controllable microstructure. Thus, the optimization of the microstructure of 2D inorganic materials including surface functional groups, layer number of nanosheets should be carried out to realize the desirable properties. Thirdly, it is still a great challenge for the fine control of electrode functionalities by using 2D materials or assembles of 2D materials in battery system because electrochemical performance of batteries is affected by many factors. [265] After introduction of 2D materials in battery system, new surfaces and/or interfaces are formed among the electrode components. As is known, the surface and interface in electrode strongly affect the mass transport; charge transfer and ions diffusion in batteries. Thus, further studies on effects of 2D inorganic materials to electrode should be performed systematically, especially in the relationship between interfacial properties of inorganic nano-sheets and their functionalities as additives from atomic level. Finally, it is very important to develop new 2D non-conductive materials with new structure and properties to fulfil the requirements in multiple fields in future.

## 4. Conclusions

In this review, we summarized the recent progress in the application of two-dimensional inorganic non-conductive materials in alkali metal-based batteries. Thanks to their excellent specific surface area and unique physical/chemical properties, two-dimensional inorganic materials have shown great potential in alkali metal-based batteries. Their non-conductive nature and special properties of the 2D structure allow them to be applied not only as additives in electrode materials but also in separators, artificial protective layers, and solid-state electrolytes. In this review, we provide a detailed account of the research progress on these materials as electrode materials or additives in alkali metal-based batteries, as well as their applications as separators, substrates for lithium/sodium/potassium metal anodes, anchoring materials in Li-S batteries, and catalytic materials in Li-O batteries.

The characteristics of two-dimensional inorganic insulating materials provide them with great potential for further development. For instance, the abundant adsorption sites for alkali metal ions make BN and g-$C_3N_4$ excellent additives for alkali metal-based ion batteries. Due to the exceptional film-forming properties of two-dimensional materials, they can even replace binders and directly form independent thin films with electrode materials. Moreover, their excellent mechanical properties, thermal stability, and ion transport properties make two-dimensional inorganic materials promising candidates as separator additives and protective layers for alkali metal-based battery anodes. The addition of materials like BN and g-$C_3N_4$ can effectively reduce the crystallinity of polymer electrolytes and enhance ion transport. Additionally, their strong anchoring and oxygen reduction capabilities make them excellent main materials or additives for sulfur cathodes and air electrodes.

To sum up, the application of two-dimensional inorganic insulating materials in lithium metal-based batteries has been widely studied, but their application in sodium/potassium metal-based batteries still needs to be further studied. There are still many obstacles to be overcome from laboratory research to industrial production Two-dimensional inorganic insulating materials offer new choices for constructing components of alkali metal-based batteries and show the potential to contribute to better battery performance. In the future, it is expected that alkali metal-based batteries with higher capacity, higher rate performance, longer cycle life, and lower cost can be achieved by optimizing the present 2D material and by using novel 2D materials.

## Author Contributions

**Yuxi Shen,** Writing Original draft. **Zengquan Zhu**, Data preparation. **Zhefeng Xu**, Supervision. **Yueming Li**, Supervision, Writing-Review & Editing, Project administration

## Conflicts of interest

"There are no conflicts to declare".

## Acknowledgements

This work was financially supported by the NSFC (Grant No. 51972281), the Natural Science Foundation of Hebei Province for Innovation Groups Program (C2022203003), and foundation of State Key Laboratory of Metastable Materials Science and Technology.

## Notes and references

Yuxi Shen, ORCID:0009-0002-3408-0670
Zengquan Zhu, ORCID: 0009-0008-2269-6295
Zhengfeng Xu, ORCID:0009-0009-7589-986X
Yueming Li, ORCID: 0000-0001-9807-4558

1. W. Zhang, Y. Huang, Y. Liu, L. Wang, S. Chou and H. Liu, *Advanced Energy Materials*, 2019, **9**, 1900464-1900486.
2. W. Cao, Q. Li, X. Yu, H. Li, Controlling Li deposition below the interface, *eScience*, 2 (2022) 47-78.
3. J. Y. Wei, X. Q. Zhang, L. P. Hou, P. Shi, B. Q. Li, Y. Xiao, C. Yan, H. Yuan and J. Q. Huang, *Advanced Materials*, 2020, **32**,2003012-200319.
4. C. Shu, J. Wang, J. Long, H. K. Liu and S. X. Dou, *Advanced Materials*, 2019, **31**, 1804587-1804630.
5. C. Yang, S. Xin, L. Mai and Y. You, *Advanced Energy Materials*, 2020, **11**, 2000974-2000991.
6. Y. Sun, J.-C. Li, H. Zhou, S. Guo, Wide-temperature-range sodium-metal batteries: from fundamentals and obstacles to optimization, *Energy & Environmental Science*, 16 (2023) 4759-4811.
7. X. Min, J. Xiao, M. Fang, W. Wang, Y. Zhao, Y. Liu, A. M. Abdelkader, K. Xi, R. V. Kumar and Z. Huang, *Energy & Environmental Science*, 2021, **14**, 2186-2243.
8. C. Chu, R. Li, F. Cai, Z. Bai, Y. Wang, X. Xu, N. Wang, J. Yang and S. Dou, *Energy & Environmental Science*, 2021, **14**, 4318-4340.
9. R. Rajagopalan, Y. Tang, X. Ji, C. Jia and H. Wang, *Advanced Functional Materials*, 2020, **30**, 1909486-1909521.
10. P. Liu and D. Mitlin, *Acc Chem Res*, 2020, **53**, 1161-1175.
11. A. Ransil, A.M. Belcher, Structural ceramic batteries using an earth-abundant inorganic waterglass binder, Nat Commun, 12 (2021) 6494.
12. Y. Shen, Z. Pu, Y. Zhang, Y. Chen, H. Zhang, N. Wang, H. Qiu and Y. Li, *Journal of Materials Chemistry A*, 2022, **10**, 17199-17207.
13. J. E. ten Elshof, H. Yuan and P. Gonzalez Rodriguez, *Advanced Energy Materials*, 2016, **6**, 1600355-1600389.
14. M. G. Rasul, A. Kiziltas, B. Arfaei and R. Shahbazian-Yassar, *npj 2D Materials and Applications*, 2021, **5**, 56.
15. J. Wang and S. Wang, *Coordination Chemistry Reviews*, 2022, **453**, 21338-21354.
16. Z. Zeng, Y. Dong, S. Yuan, W. Zhao, L. Wang, S. Liu, Y. Yang, P. Ge, W. Sun and X. Ji, *Energy Storage Materials*, 2022, **45**, 442-464.
17. S. Angizi, S. A. A. Alem, M. Hasanzadeh Azar, F. Shayeganfar, M. I. Manning, A. Hatamie, A. Pakdel and A. Simchi, *Progress in Materials Science*, 2022, **124**, 100884-100969.
18. Nahid Yaghmaeiyan a, Mahdi Mirzaei a, Reza Delghavi b, *Results in Chemistry*, 2022, **4**, 100549.
19. M. Li, Y. Zhao, Z. Ai, H. Bai, T. Zhang and S. Song, *Chemical Physics*, 2021, **550**, 111313.
20. S. Angizi, S. A. A. Alem, M. Hasanzadeh Azar, F. Shayeganfar, M. I. Manning, A. Hatamie, A. Pakdel and A. Simchi, *Progress in Materials Science*, 2022, **124**, 100884.
21. W. Paszkowicz, J. B. Pelka, M. Knapp, T. Szyszko and S. Podsiadlo, *Applied Physics A: Materials Science & Processing*, 2002, **75**, 431-435.
22. N. Izyumskaya, D. O. Demchenko, S. Das, Ü. Özgür, V. Avrutin and H. Morkoç, *Advanced Electronic Materials*, 2017, **3**.
23. G. Cassabois, P. Valvin and B. Gil, *Nature Photonics*, 2016, **10**, 262-266.
24. N. Marom, J. Bernstein, J. Garel, A. Tkatchenko, E. Joselevich, L. Kronik and O. Hod, *Physical Review Letters*, 2010, **105**, 046801.
25. S. M. Gilbert, T. Pham, M. Dogan, S. Oh, B. Shevitski, G. Schumm, S. Liu, P. Ercius, S. Aloni, M. L. Cohen and A. Zettl, *2D Materials*, 2019, **6**, 021006.
26. G. Constantinescu, A. Kuc and T. Heine, *Physical Review Letters*, 2013, **111**, 036104.
27. A. E. Naclerio and P. R. Kidambi, *Advanced Materials*, 2022, **35**.
28. E. I. Barbara Ju¨rgens, Ju¨rgen Senker, Peter Kroll, Helen Mu¨ ller, Wolfgang Schnick., *Journal of the American Chemical Society*, 2003, **125**, 10288-10300.
29. A. Hayat, A. G. Al-Sehemi, K. S. El-Nasser, T. A. Taha, A. A. Al-Ghamdi, S. Jawad Ali Shah, M. A. Amin, T. Ali, T. Bashir, A. Palamanit, J. Khan and W. I. Nawawi, *International Journal of Hydrogen Energy*, 2022, **47**, 5142-5191.
30. Q. Hao, G. Jia, W. Wei, A. Vinu, Y. Wang, H. Arandiyan and B.-J. Ni, *Nano Research*, 2019, **13**, 18-37.
31. B. He, M. Feng, X. Chen and J. Sun, *Green Energy & Environment*, 2021, **6**, 823-845.
32. N. Rono, J. K. Kibet, B. S. Martincigh and V. O. Nyamori, *Critical Reviews in Solid State and Materials Sciences*, 2021, **46**, 189-217.
33. F. Bergaya, C. Detellier, J. F. Lambert and G. Lagaly, in *Handbook of Clay Science*, 2013, pp. 655-677.
34. F. Uddin, *Metallurgical and Materials Transactions A*, 2008, **39**, 2804-2814.
35. T. Nakato and N. Miyamoto, *Materials*, 2009, **2**, 1734-1761.
36. F. Uddin, in *Current Topics in the Utilization of Clay in Industrial and Medical Applications*, 2018.
37. B. S. Kumar, A. Dhakshinamoorthy and K. Pitchumani, *Catal. Sci. Technol.*, 2014, **4**, 2378-2396.
38. W. J. Huang, J. H. Liu, Q. M. She, J. Q. Zhong, G. E. Christidis and C. H. Zhou, *Catalysis Reviews*, 2021, **65**, 929-985.
39. J. Feng, M. Liu, L. Fu, S. Ma, J. Yang, W. Mo and X. Su, *Ceramics International*, 2020, **46**, 6413-6417.
40. H. F. Muiambo, W. W. Focke, M. Atanasova and A. Benhamida, *Applied Clay Science*, 2015, **105-106**, 14-20.
41. A. N. Nguyen, L. Reinert, J. M. Lévêque, A. Beziat, P. Dehaudt, J. F. Juliaa and L. Duclaux, *Applied Clay Science*, 2013, **72**, 9-17.
42. S. İşçi, *Applied Clay Science*, 2017, **146**, 7-13.
43. H. F. Muiambo and W. W. Focke, *Molecular Crystals and Liquid Crystals*, 2012, **555**, 65-75.
44. O. Folorunso, C. Dodds, G. Dimitrakis and S. Kingman, *International Journal of Mineral Processing*, 2012, **114-117**, 69-79.
45. K. Okada, S. Matsui, T. Isobe, Y. Kameshima and A. Nakajima, *Ceramics International*, 2008, **34**, 345-350.
46. T. T. Zhu, C. H. Zhou, F. B. Kabwe, Q. Q. Wu, C. S. Li and J. R. Zhang, *Applied Clay Science*, 2019, **169**, 48-66.
47. Z. Fu, T. Liu, X. Kong, Y. Liu, J. Xu, B. Zhang, H. Chen and Z. Chen, *Materials Letters*, 2019, **238**, 175-178.
48. J.-J. Shao, K. Raidongia, A. R. Koltonow and J. Huang, *Nature*

*Communications*, 2015, **6**, 7602.
49. H. Bai, Y. Zhao, W. Wang, T. Zhang, H. Yi and S. Song, *Ceramics International*, 2019, **45**, 17054-17063.
50. H. Zhang and Y. Yao, *Environmental Chemistry Letters*, 2017, **15**, 507-513.
51. L. Zang, J. Luo, J. Guo, H. Liu and J. Ru, *Polymer Bulletin*, 2010, **65**, 669-680.
52. Y. Lin and J. W. Connell, *Nanoscale*, 2012, **4**, 6908-6939.
53. J. Wen, J. Xie, X. Chen and X. Li, *Applied Surface Science*, 2017, **391**, 72-123.
54. A. H. Alias, M. N. Norizan, F. A. Sabaruddin, M. R. M. Asyraf, M. N. F. Norrrahim, A. R. Ilyas, A. M. Kuzmin, M. Rayung, S. S. Shazleen, A. Nazrin, S. F. K. Sherwani, M. M. Harussani, M. S. N. Atikah, M. R. Ishak, S. M. Sapuan and A. Khalina, *Coatings*, 2021, **11**, 1355.
55. X. J. Yang, L. L. Li, W. L. Sang, J. L. Zhao, X. X. Wang, C. Yu, X. H. Zhang and C. C. Tang, *Journal of Alloys and Compounds*, 2017, **693**, 642-649.
56. Y. Zhang, M. Wei, Q. Fu and X. Bao, *Science Bulletin*, 2015, **60**, 1572-1579.
57. Y. Zhang, X. Weng, H. Li, H. Li, M. Wei, J. Xiao, Z. Liu, M. Chen, Q. Fu and X. Bao, *Nano Letters*, 2015, **15**, 3616-3623.
58. S. Gao, B. Li, D. Li, C. Zhang, R. Liu and S. Wang, *Ceramics International*, 2018, **44**, 11424-11430.
59. A. Kuang, T. Zhou, G. Wang, Y. Li, G. Wu, H. Yuan, H. Chen and X. Yang, *Applied Surface Science*, 2016, **362**, 562-571.
60. J.-S. Li, C.-R. Zhang and B. Li, *Applied Surface Science*, 2011, **257**, 7752-7757.
61. C. Morchutt, J. Björk, S. Krotzky, R. Gutzler and K. Kern, *Chemical Communications*, 2015, **51**, 2440-2443.
62. J. Ren, N. Zhang, H. Zhang and X. Peng, *Structural Chemistry*, 2014, **26**, 731-738.
63. S. Roth, F. Matsui, T. Greber and J. Osterwalder, *Nano Letters*, 2013, **13**, 2668-2675.
64. F. Cao, Y. Ding, L. Chen, C. Chen and Z. Fang, *Materials & Design (1980-2015)*, 2014, **54**, 610-615.
65. M. Corso, W. Auwärter, M. Muntwiler, A. Tamai, T. Greber and J. r. Osterwalder, *Science*, 2004, **303**, 217-220.
66. V. Deshmukh, M. Nagnathappa, B. Kharat and A. Chaudhari, *Journal of Molecular Liquids*, 2014, **193**, 13-22.
67. S. Duperrier, R. Chiriac, C. Sigala, C. Gervais, S. Bernard, D. Cornu and P. Miele, *Journal of the European Ceramic Society*, 2009, **29**, 851-855.
68. R. Kumar, S. Sahoo, E. Joanni, R. K. Singh, R. M. Yadav, R. K. Verma, D. P. Singh, W. K. Tan, A. Pérez del Pino, S. A. Moshkalev and A. Matsuda, *Nano Research*, 2019, **12**, 2655-2694.
69. A. Rice, A. Allerman, M. Crawford, T. Beechem, T. Ohta, C. Spataru, J. Figiel and M. Smith, *Journal of Crystal Growth*, 2018, **485**, 90-95.
70. J. Lee, A. V. Ravichandran, J. Mohan, L. Cheng, A. T. Lucero, H. Zhu, Z. Che, M. Catalano, M. J. Kim, R. M. Wallace, A. Venugopal, W. Choi, L. Colombo and J. Kim, *ACS Applied Materials & Interfaces*, 2020, **12**, 36688-36694.
71. S. Behura, P. Nguyen, S. Che, R. Debbarma and V. Berry, *Journal of the American Chemical Society*, 2015, **137**, 13060-13065.
72. R. Y. Tay, S. H. Tsang, M. Loeblein, W. L. Chow, G. C. Loh, J. W. Toh, S. L. Ang and E. H. T. Teo, *Applied Physics Letters*, 2015, **106**.
73. S. Behura, P. Nguyen, R. Debbarma, S. Che, M. R. Seacrist and V. Berry, *ACS Nano*, 2017, **11**, 4985-4994.
74. P. S. J. L. P. A. E. Sutter, *ACS Nano*, 2011, **5**, 7303-7309.
75. J. Wang and S. Wang, *Coordination Chemistry Reviews*, 2022, **453**, 214338.
76. A. Hayat, T. A. M. Taha, A. M. Alenad, L. Yingjin, S. K. B. Mane, A. Hayat, M. Khan, A. U. Rehman, W. U. Khan and N. Shaishta, *Energy Technology*, 2021, **9**, 2100091.
77. A. Hayat, T. A. Taha, A. M. Alenad, T. Ali, T. Bashir, A. Ur Rehman, I. Ullah, A. Hayat, A. Irfan and W. U. Khan, *International Journal of Energy Research*, 2021, **45**, 19921-19928.
78. A. M. Alenad, T. A. Taha, M. A. Amin, A. Irfan, J. Oliva, Y. Al-Hadeethi, A. Palamanit, M. khan, A. Hayat, S. Kumar Baburao Mane and M. Sohail, *Journal of Photochemistry and Photobiology A: Chemistry*, 2022, **423**, 113591.
79. N. F. F. Moreira, M. J. Sampaio, A. R. Ribeiro, C. G. Silva, J. L. Faria and A. M. T. Silva, *Applied Catalysis B: Environmental*, 2019, **248**, 184-192.
80. M. Sohail, T. Altalhi, A. G. Al-Sehemi, T. A. M. Taha, K. S. El-Nasser, A. A. Al-Ghamdi, M. Boukhari, A. Palamanit, A. Hayat, M. A. Amin and W. I. Nawawi Bin Wan Ismail, *Nanomaterials*, 2021, **11**, 3245.
81. Y. Liu, X. Guo, Z. Chen, W. Zhang, Y. Wang, Y. Zheng, X. Tang, M. Zhang, Z. Peng, R. Li and Y. Huang, *Applied Catalysis B: Environmental*, 2020, **266**, 118624.
82. X. Dong and F. Cheng, *Journal of Materials Chemistry A*, 2015, **3**, 23642-23652.
83. H. Huang, L. Jiang, J. Yang, S. Zhou, X. Yuan, J. Liang, H. Wang, H. Wang, Y. Bu and H. Li, *Renewable and Sustainable Energy Reviews*, 2023, **173**, 113110.
84. P. Niu, L. Zhang, G. Liu and H.-M. Cheng, *Advanced Functional Materials*, 2012, **22**, 4763-4770.
85. Y. Hong, J. Shi, W. Shi, Z. Fang, R. Chen and Y. Huang, *Carbon*, 2018, **136**, 160-167.
86. Y. Hong, E. Liu, J. Shi, X. Lin, L. Sheng, M. Zhang, L. Wang and J. Chen, *International Journal of Hydrogen Energy*, 2019, **44**, 7194-7204.
87. X. Zhang, X. Xie, H. Wang, J. Zhang, B. Pan and Y. Xie, *Journal of the American Chemical Society*, 2012, **135**, 18-21.
88. G. Li, H. Wang, X. Shi, C. Yang, R. Wang, B. He, J. Jin, Y. Gong, A. Tang and H. Yang, *Chem Commun (Camb)*, 2022, **58**, 11276-11279.
89. Y. Wang, Y. Fan, D. Liao, Y. Wu, Y. Yu and C. Hu, *Energy Storage Materials*, 2022, **51**, 212-222.
90. M. Yang, Z. Li, W. Chen, Y. Hu and Y. Yan, *Energy & Fuels*, 2020, **34**, 8947-8955.
91. L. Wu, Y. Zhao, Y. Yu, B. Liao, H. Pang and H. Xie, *Inorganic Chemistry Frontiers*, 2023, **10**, 651-665.
92. F. Jia and S. Song, *Surface Review and Letters*, 2014, **21**, 1430001.
93. Y. Zhou, A. M. LaChance, A. T. Smith, H. Cheng, Q. Liu and L. Sun, *Advanced Functional Materials*, 2019, **29**, 1807611.
94. I. Janica, S. Del Buffa, A. Mikołajczak, M. Eredia, D. Pakulski, A. Ciesielski and P. Samorì, *Nanoscale*, 2018, **10**, 23182-23190.
95. L. A. P.-M. O. B. C. J. P. J. L. PeÂrez-RodrõÂguez, *Phys Chem Minerals* 2001, **28**, 61-66.
96. J. B. Goodenough and Y. Kim, *Journal of Power Sources*, 2011, **196**, 6688-6694.
97. L. Zhang, X. Li, M. Yang and W. Chen, *Energy Storage Materials*, 2021, **41**, 522-545.
98.H. Li, R. Y. Tay, S. H. Tsang, W. Liu and E. H. T. Teo, *Electrochimica Acta*, 2015, **166**, 197-205.
99. D. Jia, R. Tong, L. Ning, Z. Yang, Y. Zhang, W. Gu and X. Liu, *Journal of Alloys and Compounds*, 2021, **857**, 157571.
100. C. Chowdhury, S. Karmakar and A. Datta, *ACS Energy Letters*, 2016, **1**, 253-259.
101. J. Bao, L. Zhu, H. Wang, S. Han, Y. Jin, G. Zhao, Y. Zhu, X. Guo, J. Hou, H. Yin and J. Tian, *The Journal of Physical Chemistry C*, 2018, **122**, 23329-23335.
102. S. Kansara, S. K. Gupta, Y. Sonvane, M. V. Pajtler and R. Ahuja, *The Journal of Physical Chemistry C*, 2019, **123**, 19340-19346.
103. M. Waqas, S. Ali, D. Chen, B. Boateng, Y. Han, M. Zhang, J. Han, J. B. Goodenough and W. He, *Composites Part B: Engineering*, 2019, **177**, 107448.
104. M. Waqas, S. Ali, W. Lv, D. Chen, B. Boateng and W. He,

*Advanced Materials Interfaces*, 2019, **6**, 1801330.
105. D. Cao, Q. Zhang, A. M. Hafez, Y. Jiao, Y. Ma, H. Li, Z. Cheng, C. Niu and H. Zhu, *Small Methods*, 2019, **3**, 1800539.
106. S. Liu, J. Zhao, F. Li, Y. Zhao and G. Li, *Journal of Materials Chemistry A*, 2022, **10**, 5221-5229.
107.
108. L. Shi, A. Xu and T. Zhao, *ACS Appl Mater Interfaces*, 2017, **9**, 1987-1994.
109. K. Yan, H. W. Lee, T. Gao, G. Zheng, H. Yao, H. Wang, Z. Lu, Y. Zhou, Z. Liang, Z. Liu, S. Chu and Y. Cui, *Nano Lett*, 2014, **14**, 6016-6022.
110. G. Li, H. Li, Y. Wang, D. Xiong, S. Wang, Y. Yan, S. Chen, B. Tian and Y. Shi, *ACS Appl Mater Interfaces*, 2021, **13**, 56109-56115.
111. S. Wang, L. Zhang, X. Cai, T. Chu, D. Liu, C. Han, X. Qin, F. Kang and B. Li, *Journal of Materials Chemistry A*, 2021, **9**, 25004-25012.
112. W. Luo, L. Zhou, K. Fu, Z. Yang, J. Wan, M. Manno, Y. Yao, H. Zhu, B. Yang and L. Hu, *Nano Lett*, 2015, **15**, 6149-6154.
113. Y. Liu, Y. Qiao, Y. Zhang, Z. Yang, T. Gao, D. Kirsch, B. Liu, J. Song, B. Yang and L. Hu, *Energy Storage Materials*, 2018, **12**, 197-203.
114. J. Sheng, Q. Zhang, M. Liu, Z. Han, C. Li, C. Sun, B. Chen, X. Zhong, L. Qiu and G. Zhou, *Nano Lett*, 2021, **21**, 8447-8454.
115. J. Wu, X. Li, Z. Rao, X. Xu, Z. Cheng, Y. Liao, L. Yuan, X. Xie, Z. Li and Y. Huang, *Nano Energy*, 2020, **72**, 104725.
116. J. Shim, H. J. Kim, B. G. Kim, Y. S. Kim, D.-G. Kim and J.-C. Lee, *Energy & Environmental Science*, 2017, **10**, 1911-1916.
117. M. G. Rasul, M. Cheng, Y. Jiang, Y. Pan and R. Shahbazian-Yassar, *ACS Nanosci Au*, 2022, **2**, 297-306.
118. Y. Zhao, Y. Qin, X. Da, X. Weng, Y. Gao, G. Gao, Y. Su and S. Ding, *ChemSusChem*, 2022, **15**, e202201554.
119. B. Shen, T. W. Zhang, Y. C. Yin, Z. X. Zhu, L. L. Lu, C. Ma, F. Zhou and H. B. Yao, *Chem Commun (Camb)*, 2019, **55**, 7703-7706.
120. X. Zhang, W. Guo, L. Zhou, Q. Xu and Y. Min, *Journal of Materials Chemistry A*, 2021, **9**, 20530-20543.
121. Y. Li, L. Zhang, Z. Sun, G. Gao, S. Lu, M. Zhu, Y. Zhang, Z. Jia, C. Xiao, H. Bu, K. Xi and S. Ding, *Journal of Materials Chemistry A*, 2020, **8**, 9579-9589.
122. J. Yin, X. Xu, S. Jiang, Y. Lei and Y. Gao, *Journal of Power Sources*, 2022, **550**, 232139.
123. J. Li, L. Yang, H. Zhang and X. Ji, *Chemical Engineering Journal*, 2022, **438**, 135418.
124. Z. Zhang, A. R. Gonzalez and K. L. Choy, *ACS Applied Energy Materials*, 2019, **2**, 7438-7448.
125. Q. Cheng, A. Li, N. Li, S. Li, A. Zangiabadi, T.-D. Li, W. Huang, A. C. Li, T. Jin, Q. Song, W. Xu, N. Ni, H. Zhai, M. Dontigny, K. Zaghib, X. Chuan, D. Su, K. Yan and Y. Yang, *Joule*, 2019, **3**, 1510-1522.
126. L. Zhu, Y. Wang, Y. Wu, W. Feng, Z. Liu, W. Tang, X. Wang and Y. Xia, *Advanced Functional Materials*, 2022, **32**, 2201136.
127. J.-H. Kim, D.-H. Park, J.-S. Jang, J.-H. Shin, M.-C. Kim, S.-B. Kim, S.-H. Moon, S.-N. Lee and K.-W. Park, *Chemical Engineering Journal*, 2022, **446**, 137035.
128. Y. Zhao, L. Yang, J. Zhao, Q. Cai and P. Jin, *Phys Chem Chem Phys*, 2017, **19**, 18208-18216.
129. Y. Yi, H. Li, H. Chang, P. Yang, X. Tian, P. Liu, L. Qu, M. Li, B. Yang, H. Li, W. Zhu and S. Dai, *Chemistry*, 2019, **25**, 8112-8117.
130. D. Gao, Y. Li, Z. Guo, Z. Liu, K. Guo, Y. Fang, Y. Xue, Y. Huang and C. Tang, *Journal of Alloys and Compounds*, 2021, **887**, 161273.
131. D. R. Deng, F. Xue, C. D. Bai, J. Lei, R. Yuan, M. S. Zheng and Q. F. Dong, *ACS Nano*, 2018, **12**, 11120-11129.
132. Y. Fan, Z. Yang, W. Hua, D. Liu, T. Tao, M. M. Rahman, W. Lei, S. Huang and Y. Chen, *Advanced Energy Materials*, 2017, **7**, 1602380.
133. Y. Mussa, Z. Bayhan, N. Althubaiti, M. Arsalan and F. Alsharaeh, *Materials Chemistry and Physics*, 2021, **257**, 123807.
134. W. Gao, Y. Liu, C. Cao, Y. Zhang, Y. Xue and C. Tang, *J Colloid Interface Sci*, 2022, **610**, 527-537.
135. B. He, W.-C. Li, Y. Zhang, X.-F. Yu, B. Zhang, F. Li and A.-H. Lu, *Journal of Materials Chemistry A*, 2018, **6**, 24194-24200.
136. K. Zhu, P. Xue, G. Cheng, M. Wang, H. Wang, C. Bao, K. Zhang, Q. Li, J. Sun, S. Guo, Y. Yao and C.-P. Wong, *Energy Storage Materials*, 2021, **43**, 130-142.
137. H. S. Kim, H. J. Kang, H. Lim, H. J. Hwang, J. W. Park, T. G. Lee, S. Y. Cho, S. G. Jang and Y. S. Jun, *Nanomaterials (Basel)*, 2021, **12**, 11.
138. P. J. H. Kim, J. Seo, K. Fu, J. Choi, Z. Liu, J. Kwon, L. Hu and U. Paik, *NPG Asia Materials*, 2017, **9**, e375-e375.
139. Y. Fan, D. Liu, M. M. Rahman, T. Tao, W. Lei, S. Mateti, B. Yu, J. Wang, C. Yang and Y. Chen, *ACS Applied Energy Materials*, 2019, **2**, 2620-2628.
140. J. Zhang, W. Ma, Z. Feng, F. Wu, D. Wei, B. Xi and S. Xiong, *Journal of Energy Chemistry*, 2019, **39**, 54-60.
141. T. Wu, T. Yang, J. Zhang, X. Zheng, K. Liu, C. Wang and M. Chen, *Journal of Energy Chemistry*, 2021, **59**, 220-228.
142. X. Fan, Y. Liu, J. Tan, S. Yang, X. Zhang, B. Liu, H. Cheng, Z. Sun and F. Li, *Journal of Materials Chemistry A*, 2022, **10**, 7653-7659.
143. X. Xu, L. Wang, H. Fei and L. Ci, *Journal of Materials Science: Materials in Electronics*, 2019, **30**, 19119-19125.
144. X. Yin, L. Wang, Y. Kim, N. Ding, J. Kong, D. Safanama, Y. Zheng, J. Xu, D. V. M. Repaka, K. Hippalgaonkar, S. W. Lee, S. Adams and G. W. Zheng, *Adv Sci (Weinh)*, 2020, **7**, 2001303.
145. D. Adekoya, S. Zhang and M. Hankel, *Carbon*, 2021, **176**, 480-487.
146. Y. Qian, H. Lai, J. Ma, G. Deng, B. Long, T. Song, L. Liu, X. Wang and Y. Tong, *J Colloid Interface Sci*, 2022, **606**, 537-543.
147. K. Liu, J. Man, J. Cui, H. Zhang, T. Li, J. Yang, Z. Wen and J. Sun, *Materials Letters*, 2019, **234**, 117-120.
148. J. Xu, Y. Xu, G. Tang, H. Tang and H. Jiang, *Applied Surface Science*, 2019, **492**, 37-44.
149. H. Tran Huu, X. D. Nguyen Thi, K. Nguyen Van, S. J. Kim and V. Vo, *Materials (Basel)*, 2019, **12**, 1730.
150. D. Versaci, J. Amici, C. Francia and S. Bodoardo, *Solid State Ionics*, 2020, **346**, 115210.
151. Y. Zuo, X. Xu, C. Zhang, J. Li, R. Du, X. Wang, X. Han, J. Arbiol, J. Llorca, J. Liu and A. Cabot, *Electrochimica Acta*, 2020, **349**, 136369.
152. D. D. Pathak, D. P. Dutta, B. R. Ravuri, A. Ballal, A. C. Joshi and A. K. Tyagi, *Electrochimica Acta*, 2021, **370**, 137715.
153. H. Tran Huu, H. T. T. Le, T. Huong Nguyen, L. Nguyen Thi, V. Vo and W. Bin Im, *Applied Surface Science*, 2021, **549**, 149312.
154. V. Vo, X. D. Nguyen Thi, Y.-S. Jin, G. Ly Thi, T. T. Nguyen, T. Q. Duong and S.-J. Kim, *Chemical Physics Letters*, 2017, **674**, 42-47.
155. H. H. Tran, P. H. Nguyen, V. H. Cao, L. T. Nguyen, V. M. Tran, M. L. Phung Le, S.-J. Kim and V. Vo, *Chemical Physics Letters*, 2019, **715**, 284-292.
156. Q. D. Le, P. N. Ngoc, H. T. Huu, T. H. T. Nguyen, T. N. Van, L. N. Thi, M. K. Le, V. M. Tran, M. L. P. Le and V. Vo, *Chemical Physics Letters*, 2022, **796**, 139550.
157. Y. Liu, S. He, Y. Zhong, X. Xu and Z. Shao, *Journal of Alloys and Compounds*, 2019, **805**, 522-530.
158. H. S. H. Mohamed, C.-F. Li, L. Wu, W.-H. Shi, W.-D. Dong, J. Liu, Z.-Y. Hu, L.-H. Chen, Y. Li and B.-L. Su, *Chemical Engineering Journal*, 2021, **407**, 126941.
159. P. Zhang, B. Cai, Y. Feng, H. Pan and J. Yao, *Journal of Alloys and Compounds*, 2021, **875**, 160077.
160. H. Xu, L. Sun, W. Li, M. Gao, Q. Zhou, P. Li, S. Yang and J.

Lin, *Chemical Engineering Journal*, 2022, **435**, 135129.
161. S. Wang, Y. Shi, C. Fan, J. Liu, Y. Li, X. L. Wu, H. Xie, J. Zhang and H. Sun, *ACS Appl Mater Interfaces*, 2018, **10**, 30330-30336.
162. W. Kong, J. Yu, X. Shi, J. Yin, H. Yang and Z. Wen, *Journal of The Electrochemical Society*, 2020, **167**, 060518.
163. S. Kang, X. Li, C. Yin, J. Wang, M. S. Aslam, H. Qi, Y. Cao, J. Jin and L. Cui, *J Colloid Interface Sci*, 2019, **554**, 269-277.
164. H. Zhang, J. Yin, Y. Liu, Z. Lang, Y. Liu, W. He, L. Ma, J. Cui and J. Sun, *Journal of Electroanalytical Chemistry*, 2020, **862**, 114004.
165. H. Zuhaib, M. Munisamy, N. Perumal, H.-W. Yang, W. S. Kang and S.-J. Kim, *Materials Chemistry and Physics*, 2023, **298**, 127463.
166. L. Wan, Y. Tang, L. Chen, K. Wang, J. Zhang, Y. Gao, J. Y. Lee, T. Lu, X. Xu, J. Li, Y. Zheng and L. Pan, *Chemical Engineering Journal*, 2021, **410**, 128349.
167. G. M. Weng, Y. Xie, H. Wang, C. Karpovich, J. Lipton, J. Zhu, J. Kong, L. D. Pfefferle and A. D. Taylor, *Angew Chem Int Ed Engl*, 2019, **58**, 13727-13733.
168. K. Sun, Y. Wang, C. Chang, S. Yang, S. Di, P. Niu, S. Wang and L. Li, *Chemical Engineering Journal*, 2021, **425**, 131591.
169. H. Shi, S. Wang, Y. Xia, X. Yan, D. Wang, Y. Yin, P. Huai, Z. Xu, C. Min, S. Liu and X. Wu, *ACS Applied Energy Materials*, 2022, **5**, 7308-7316.
170. H. L. Tran Huu, Hang T. T. Nguyen, Thanh Huong Nguyen Thi, Lan Vo, Vien Im, Won Bin., *International Journal of Energy Research*, 2021, **46**, 3233-3248.
171. D. Adekoya, M. Li, M. Hankel, C. Lai, M.-S. Balogun, Y. Tong and S. Zhang, *Energy Storage Materials*, 2020, **25**, 495-501.
172. J. Wu, L. Tian, H. Duan, Y. Cheng and L. Shi, *ACS Appl Mater Interfaces*, 2021, **13**, 46821-46829.
173. Y. Jeon, S. Kang, S. H. Joo, M. Cho, S. O. Park, N. Liu, S. K. Kwak, H.-W. Lee and H.-K. Song, *Energy Storage Materials*, 2020, **31**, 505-514.
174. Z. Lu, Q. Liang, B. Wang, Y. Tao, Y. Zhao, W. Lv, D. Liu, C. Zhang, Z. Weng, J. Liang, H. Li and Q.-H. Yang, *Advanced Energy Materials*, 2019, **9**, 1803186.
175. W. Lu, H. Yang, J. Chen, C. Sun and F. Li, *Science China Materials*, 2021, **64**, 2675-2682.
176. Z. Zhuang, B. Ju, P. Ma, L. Yang and F. Tu, *Ionics*, 2021, **27**, 1069-1079.
177. Y. Xu, T. Li, L. Wang and Y. Kang, *Adv Mater*, 2019, **31**, e1901662.
178. F. Zhao, P. Zhai, Y. Wei, Z. Yang, Q. Chen, J. Zuo, X. Gu and Y. Gong, *Adv Sci (Weinh)*, 2022, **9**, e2103930.
179. H. Zhang, Y. Wang, S. Ju, P. Gao, T. Zou, T. Zhang, J. Wang, G. Xia and X. Yu, *Energy Storage Materials*, 2022, **52**, 220-229.
180. X. Luan, C. Wang, C. Wang, X. Gu, J. Yang and Y. Qian, *ACS Appl Mater Interfaces*, 2020, **12**, 11265-11272.
181. Y. Roh, J. Song, J.-H. Lee, H. Kwon, J. Baek, D. Shin, Y. G. Yoo, S. Ha, W. Kim, K. Ryu and H.-T. Kim, *Energy Storage Materials*, 2022, **51**, 777-788.
182. J. Hu, J. Tian and C. Li, *ACS Appl Mater Interfaces*, 2017, **9**, 11615-11625.
183. J. Li, L. Zhu, H. Xie, W. Zheng and K. Zhang, *Colloids and Surfaces A: Physicochemical and Engineering Aspects*, 2023, **657**, 130520.
184. Q. Zhang, Q. Wang, S. Huang, Y. Jiang and Z. Chen, *Inorganic Chemistry Communications*, 2021, **131**, 108793.
185. X. Hao, K. Chen, Y. Tang, X. Zhong and K. Cai, *Journal of Alloys and Compounds*, 2023, **942**, 169064.
186. H. Liang, S. Wang, Q. Ye, C. Zeng, Z. Tong, Y. Ma and H. Li, *Chem Commun (Camb)*, 2022, **58**, 10821-10824.
187. J. Wei, X. Zheng, W. Lin, Y. Si, K. Ji, C. Wang and M. Chen, *Journal of Alloys and Compounds*, 2022, **909**, 164825.
188. Y. Huang, B. Chen, J. Duan, F. Yang, T. Wang, Z. Wang, W. Yang, C. Hu, W. Luo and Y. Huang, *Angew Chem Int Ed Engl*, 2020, **59**, 3699-3704.
189. Z. Guo, C. Ye, T. Zhao, W. Wu, W. Kou, Y. Zhang, W. Dong, W. Li and J. Wang, *Journal of Power Sources*, 2023, **562**, 232784.
190. Q. Pang and L. F. Nazar, *ACS Nano*, 2016, **10**, 4111-4118.
191. Q. Pang, X. Liang, C. Y. Kwok, J. Kulisch and L. F. Nazar, *Advanced Energy Materials*, 2016, **7**, 1601630.
192. Y. Zheng, H. Li, H. Yuan, H. Fan, W. Li and J. Zhang, *Applied Surface Science*, 2018, **434**, 596-603.
193. Y. Gong, C. Fu, G. Zhang, H. Zhou and Y. Kuang, *Electrochimica Acta*, 2017, **256**, 1-9.
194. J. Zhang, J.-Y. Li, W.-P. Wang, X.-H. Zhang, X.-H. Tan, W.-G. Chu and Y.-G. Guo, *Advanced Energy Materials*, 2018, **8**, 1702839.
195. J. Wang, Z. Meng, W. Yang, X. Yan, R. Guo and W. Q. Han, *ACS Appl Mater Interfaces*, 2019, **11**, 819-827.
196. Z. Jia, H. Zhang, Y. Yu, Y. Chen, J. Yan, X. Li and H. Zhang, *Journal of Energy Chemistry*, 2020, **43**, 71-77.
197. L. Qu, P. Liu, Y. Yi, T. Wang, P. Yang, X. Tian, M. Li, B. Yang and S. Dai, *ChemSusChem*, 2019, **12**, 213-223.
198. P. Song, Z. Chen, Y. Chen, Q. Ma, X. Xia and H. Liu, *Electrochimica Acta*, 2020, **363**, 137217.
199. X. Wang, G. Li, M. Li, R. Liu, H. Li, T. Li, M. Sun, Y. Deng, M. Feng and Z. Chen, *Journal of Energy Chemistry*, 2021, **53**, 234-240.
200. Y. Li, M. Chen, P. Zeng, H. Liu, H. Yu, Z. Luo, Y. Wang, B. Chang and X. Wang, *Journal of Alloys and Compounds*, 2021, **873**, 159883.
201. H. Pan, X. Huang, C. Wang, D. Liu, D. Wang, R. Zhang, S. Li, C. Lv, L. Zhao, J. Wang and X. Huang, *Chemical Engineering Journal*, 2021, **410**, 128424.
202. S.-H. Moon, J.-H. Shin, J.-H. Kim, J.-S. Jang, S.-B. Kim, Y.-Y. Park, S.-N. Lee and K.-W. Park, *Materials Chemistry and Physics*, 2022, **287**, 126267.
203. H. Zhang, X. Lin, J. Li, T. Han, M. Zhu, X. Xu, C. Hu and J. Liu, *Journal of Alloys and Compounds*, 2021, **881**, 160629.
204. G. Xu, L. Li, M. Li, C. Xi, J. Yan, R. Li, Y. Chao, C. Yang and Y. Yu, *Applied Surface Science*, 2022, **604**, 154556.
205. E. Abd-Alkuder Salman, K. Abaid Samawi, M. Fawzi Nassar, G. Abdulkareem-Alsultan and E. Abdulmalek, *Journal of Electroanalytical Chemistry*, 2023, **945**, 117629.
206. W.-W. Liu, S.-T. Niu, Z.-Q. Xu, R. Zou, C.-Y. Cui, Y.-X. Lei, X.-B. Zhang and F. Ran, *Applied Surface Science*, 2023, **609**, 155327.
207. S. Majumder, M. Shao, Y. Deng and G. Chen, *Journal of Power Sources*, 2019, **431**, 93-104.
208. H. Zou, Y. Zou, Y. Lv, Z. Ao, N. Chen and Y. Huang, *ACS Applied Energy Materials*, 2022, **5**, 10067-10075.
209. M. Chen, X. Zhao, Y. Li, P. Zeng, H. Liu, H. Yu, M. Wu, Z. Li, D. Shao, C. Miao, G. Chen, H. Shu, Y. Pei and X. Wang, *Chemical Engineering Journal*, 2020, **385**, 123905.
210. Y. Wang, L. Yang, Y. Chen, Q. Li, C. Chen, B. Zhong, X. Guo, Z. Wu and G. Wang, *ACS Appl Mater Interfaces*, 2020, **12**, 57859-57869.
211. M. Luo, Y. Bai, R. Sun, Z. Wang, W. Sun, P. Lin, X. Dai and K. Sun, *Industrial & Engineering Chemistry Research*, 2021, **60**, 1231-1240.
212. W. B. Luo, S. L. Chou, J. Z. Wang, Y. C. Zhai and H. K. Liu, *Small*, 2015, **11**, 2817-2824.
213. Q. Liu and J. Zhang, *Langmuir*, 2013, **29**, 3821-3828.
214. M.-Q. Wang, W.-H. Yang, H.-H. Wang, C. Chen, Z.-Y. Zhou and S.-G. Sun, *ACS Catalysis*, 2014, **4**, 3928-3936.
215. X. Zou, J. Su, R. Silva, A. Goswami, B. R. Sathe and T. Asefa, *Chem Commun (Camb)*, 2013, **49**, 7522-7524.
216. Y. Wu, T. Wang, Y. Zhang, S. Xin, X. He, D. Zhang and J. Shui, *Sci Rep*, 2016, **6**, 24314.
217. X. Li, Y. Zhao, L. Ding, D. Wang, Q. Guo, Z. Li, H. Luo, D.

Zhang and Y. Yu, *Nanomaterials (Basel)*, 2021, **11**, 1088.
218. W. Zhao, J. Wang, R. Yin, B. Li, X. Huang, L. Zhao and L. Qian, *J Colloid Interface Sci*, 2020, **564**, 28-36.
219. R. Cao, Y. Cui, G. Huang, W. Liu, J. Liu and X. Zhang, *Nano Research*, 2023, **16**, 8405-8410.
220. E. Lokcu, N. Kacar, M. Cayirli, R. C. Ozden and M. Anik, *ACS Appl Mater Interfaces*, 2022, **14**, 34583-34592.
221. W. Chen, T. Lei, W. Lv, Y. Hu, Y. Yan, Y. Jiao, W. He, Z. Li, C. Yan and J. Xiong, *Adv Mater*, 2018, e1804084.
222. C. Chen, Y. Ma and C. Wang, *Sustainable Materials and Technologies*, 2019, **19**, e00086.
223. M. S. Chen, W. Fu, Y. Hu, M. Y. Chen, Y. J. Chiou, H. M. Lin, M. Zhang and Z. Shen, *Nanoscale*, 2020, **12**, 16262-16269.
224. J. Nunes-Pereira, A. C. Lopes, C. M. Costa, R. Leones, M. M. Silva and S. Lanceros-Méndez, *Electroanalysis*, 2012, **24**, 2147-2156.
225. M. Raja, T. P. Kumar, G. Sanjeev, L. Zolin, C. Gerbaldi and A. M. Stephan, *Ionics*, 2014, **20**, 943-948.
226. C. Fang, S. Yang, X. Zhao, P. Du and J. Xiong, *Materials Research Bulletin*, 2016, **79**, 1-7.
227. M. L. Para, D. Versaci, J. Amici, M. F. Caballero, M. V. Cozzarin, C. Francia, S. Bodoardo and M. Gamba, *Journal of Electroanalytical Chemistry*, 2021, **880**, 114876.
228. M. Carter, M. H. Parekh, V. Tomar, J. E. Dietz and V. G. Pol, *Applied Clay Science*, 2021, **208**, 106111.
229. P. Xu, X. Yan, Y. Zhou, C. Wang, H. Cheng and Y. Zhang, *Soft Matter*, 2022, **18**, 2522-2527.
230. Y. Yang, B. Yang, M. Luo, Y. Yang, Y. Wang, J. Miao, S. Wang, Z. Zheng, J. Qian, R. Xia, Y. Ke and Y. Tu, *Electrochimica Acta*, 2023, **446**, 142074.
231. M. Wang, F. Zhao, Z. Guo and S. Dong, *Electrochimica Acta*, 2004, **49**, 3595-3602.
232. S. Kim and S.-J. Park, *Solid State Ionics*, 2007, **178**, 973-979.
233. S. Kim, E.-J. Hwang, Y. Jung, M. Han and S.-J. Park, *Colloids and Surfaces A: Physicochemical and Engineering Aspects*, 2008, **313-314**, 216-219.
234. M. Xie, L. Li, K. Yuan, Y. Ma and B. Liu, *Journal of Materials Science: Materials in Electronics*, 2018, **30**, 2030-2036.
235. H. Zhao, W. Kang, N. Deng, M. Liu and B. Cheng, *Chemical Engineering Journal*, 2020, **384**, 123312.
236. M. Wang, Y. Li, S.-Y. Li, X.-X. Jia, B. Nie, H.-T. Sun, Y.-Y. Wang and J. Zhu, *Rare Metals*, 2023, **42**, 2157-2165.
237. Q. Ma, X. Sun, P. Liu, Y. Xia, X. Liu and J. Luo, *Angew Chem Int Ed Engl*, 2019, **58**, 6200-6206.
238. Y. Nan, S. Li, C. Han, H. Yan, Y. Ma, J. Liu, S. Yang and B. Li, *Advanced Functional Materials*, 2021, **31**, 2102336.
239. T. Zeng, Y. Yan, M. He, D. Du, X. Wen, B. Zhou and C. Shu, *Journal of Materials Chemistry A*, 2022, **10**, 23712-23721.
240. Y. Feng, B. Zhong, R. Zhang, M. Peng, Z. Hu, Z. Wu, N. Deng, W. Zhang and K. Zhang, *Advanced Energy Materials*, 2023, **13**, 2203912.
241. X.-Q. Xu, F.-N. Jiang, S.-J. Yang, Y. Xiao, H. Liu, F. Liu, L. Liu and X.-B. Cheng, *Journal of Energy Chemistry*, 2022, **69**, 205-210.
242. J. Zhao, D. Chen, B. Boateng, G. Zeng, Y. Han, C. Zhen, J. B. Goodenough and W. He, *Journal of Power Sources*, 2020, **451**, 227773.
243. M. Yang, N. Jue, Y. Chen and Y. Wang, *Nanoscale Res Lett*, 2021, **16**, 52.
244. Y. Zhai, X. Wang, Y. Chen, X. Sang, H. Liu, J. Sheng, Y. Wu, X. Wang and L. Li, *Journal of Membrane Science*, 2021, **621**, 118996.
245. L. Pan, H. He and H. He, *Materials Today Energy*, 2022, **26**, 101015.
246. W. Chen, Y. Hu, W. Lv, T. Lei, X. Wang, Z. Li, M. Zhang, J. Huang, X. Du, Y. Yan, W. He, C. Liu, M. Liao, W. Zhang, J. Xiong and C. Yan, *Nat Commun*, 2019, **10**, 4973.
247. Y. M. Jeon, S. Kim, M. Lee, W. B. Lee and J. H. Park, *Advanced Energy Materials*, 2020, **10**, 2003114.
248. Y. Wang, X. Li, Y. Qin, D. Zhang, Z. Song and S. Ding, *Nano Energy*, 2021, **90**, 106490.
249. H. Porthault, C. Calberg, J. Amiran, S. Martin, C. Páez, N. Job, B. Heinrichs, D. Liquet and R. Salot, *Journal of Power Sources*, 2021, **482**, 229055.
250. W. Y. Li, Z. H. Luo, X. Long, J. Y. Long, C. Pang, H. Li, X. Zhi, B. Shi, J. J. Shao and Y. B. He, *ACS Appl Mater Interfaces*, 2021, **13**, 51107-51116.
251. W. Tang, S. Tang, X. Guan, X. Zhang, Q. Xiang and J. Luo, *Advanced Functional Materials*, 2019, **29**, 1900648.
252. Y. Zhang, J. Huang, H. Liu, W. Kou, Y. Dai, W. Dang, W. Wu, J. Wang, Y. Fu and Z. Jiang, *Advanced Energy Materials*, 2023, **13**, 2300156.
253. W. Ahn, S. N. Lim, D. U. Lee, K.-B. Kim, Z. Chen and S.-H. Yeon, *Journal of Materials Chemistry A*, 2015, **3**, 9461-9467.
254. Y. Yang, G. Meng, H. Wang, W. Wang and J. Zhang, *Chemical Engineering Journal*, 2023, **451**, 138914.
255. X. Long, Z.-H. Luo, W.-H. Zhou, S.-K. Zhu, Y. Song, H. Li, C.-N. Geng, B. Shi, Z.-Y. Han, G.-M. Zhou, W. Lv and J.-J. Shao, *Energy Storage Materials*, 2022, **52**, 120-129.
256. M. Yang, J. Nan, W. Chen, A. Hu, H. Sun, Y. Chen and C. Wu, *Electrochemistry Communications*, 2021, **125**, 106971.
257. W. Wang, Y. Yang, H. Luo and J. Zhang, *J Colloid Interface Sci*, 2022, **614**, 593-602.
258. W. Wang, K. Xi, B. Li, H. Li, S. Liu, J. Wang, H. Zhao, H. Li, A. M. Abdelkader, X. Gao and G. Li, *Advanced Energy Materials*, 2022, **12**, 2200160.
259. F. Wu, H. Lv, S. Chen, S. Lorger, V. Srot, M. Oschatz, P. A. van Aken, X. Wu, J. Maier and Y. Yu, *Advanced Functional Materials*, 2019, **27**, 1902820.
260. R. Xu, Y. Sun, Y. Wang, J. Huang and Q. Zhang, *Chinese Chemical Letters*, 2017, **28**, 2235-2238.
261. P. Zhai, N. Peng, Z. Sun, W. Wu, W. Kou, G. Cui, K. Zhao and J. Wang, *Journal of Materials Chemistry A*, 2020, **8**, 23344-23353.
262. Z. Xiao, R. Wang, D. Jiang, Z. Qian, Y. Li, K. Yang, Y. Sun, Z. Zeng, F. Wu, Recent Developments of Two-Dimensional Anode Materials and Their Composites in Lithium-Ion Batteries, ACS Applied Energy Materials, 4 (2021) 7440-7461.
263. M.G. Rasul, A. Kiziltas, B. Arfaei, R. Shahbazian-Yassar, 2D boron nitride nanosheets for polymer composite materials, npj 2D Materials and Applications, 5 (2021).
264. S.A. Thomas, M.R. Pallavolu, M.E. Khan, J. Cherusseri, Graphitic carbon nitride (g-C3N4): Futuristic material for rechargeable batteries, Journal of Energy Storage, 68 (2023).
265. L. Wu, X. He, Y. Zhao, K. Huang, Z. Tong, B. Liao, H. Pang, Montmorillonite-based materials for electrochemical energy storage, Green Chemistry, 26 (2024) 678-704.

View Article Online
DOI: 10.1039/D4YA00209A

ARTICLE



**Table 1** The application of 2D inorganic non-conductive materials as additives in alkali-ion/S batteries

| *Material* | *Additives* | *Capacity* | *Rate capacity* | *Cycling stability* | *Ref.* |
|---|---|---|---|---|---|
| ***1. BN*** | | | | | |
| rGO/BN thin film | LIBs-anode | At 0.1 A $g^{-1}$,278 mAh $g^{-1}$ | At 1 A $g^{-1}$ 121 mAh $g^{-1}$ | About 100%,200cycles | 95 |
| MOF-5/BNNs | LIBs-anode | At 0.1A $g^{-1}$,1050 mAh $g^{-1}$ | At 2 A $g^{-1}$ 409 mAh $g^{-1}$ | About 100%, 1000 cycles | 96 |
| PVH–LaO/PVH-BN | LIBs-separator | At 0.5 C,158 mAh $g^{-1}$ (Based LFP) | At 20 C, 78 mAh $g^{-1}$ | 96 %, 1500 cycles | 100 |
| PE-BN/PVDF-HFP | LIBs-separator | At 2 C,120 mAh $g^{-1}$ (Based LFP) | At 4 C, 108 mAh $g^{-1}$ | 95 %, 500 cycles | 101 |
| v-BN | Li-S-cathode | At 0.2 C, 1262 mAh $g^{-1}$ (1C=1675 mA $g^{-1}$) | At 1 C, 699 mAh $g^{-1}$ | 58 %, 500 cycles | 125 |
| BN/graphene | Li-S-cathode | At 0.1C, 1553 mAh $g^{-1}$ | At 2 C, 914 mAh $g^{-1}$ | 90 %, 500 cycles | 127 |
| FBN/graphene | Li-S-cathode | At 0.2 C, 1125 mAh $g^{-1}$ | At 6 C, 556 mAh $g^{-1}$ | 93 %, 1000 cycles | 128 |
| S-BN@rGO | Li-S-cathode | At 0.2 C, 1137 mAh $g^{-1}$ | At 5 C,523 mAh $g^{-1}$ | 73 %, 500 cycles | 130 |
| BN/CNTs | Li-S-cathode | At 0.2 C, 1374 mAh $g^{-1}$ | At 4 C, 840 mAh $g^{-1}$ | 77 %, 500 cycles | 131 |
| f-BNNS/f-CNTs | Li-S-cathode | At 0.2 C, 1136 mAh $g^{-1}$ | At 5 C, 430 mAh $g^{-1}$ | Above 100%, 500 cycles | 132 |
| BN-carbon separator | Li-S-separator | At 0.5 C, 1018 mAh $g^{-1}$ | At 4 C, 780 mAh $g^{-1}$ | 76 %, 250 cycles | 134 |
| FBN separator | Li-S-separator | At 0.2 C, 1486 mAh $g^{-1}$ | At 7 C, 718 mAh $g^{-1}$ | 89 %, 1000 cycles | 135 |
| BN-P@GO | Li-S-separator | At 0.2 C, 1092 mAh $g^{-1}$ | At 3 C, 626 mAh $g^{-1}$ | 59 %, 500 cycles | 136 |
| CoB/BN@rGO | Li-S-separator | At 0.35 mA $cm^{-2}$, 1450 mAh $g^{-1}$ | At 8.7 mA $cm^{-2}$, 480.2 mAh $g^{-1}$ | 77 %, 700 cycles | 137 |
| BN/SWCNT | Li-S-separator | At 0.1 C, 1124 mAh $g^{-1}$ | -- | -,100 cycles | 138 |
| BN/PVdF | Li-S-separator | At 0.1 C, 1228 mAh $g^{-1}$ | At 1C, 791 mAh $g^{-1}$ | 90 %, 200 cycles | 139 |
| BN doped $Li_7P_3S_{11}$ | Li-S-SSEs | At 0.05 C, 803 mAh $g^{-1}$ | -- | 22 %, 50 cycles | 140 |
| BN-PEO-PVDF | Li-S-SSEs | At 0.05 C, 1000 mAh $g^{-1}$ | At 0.5 C, 400 mAh $g^{-1}$ | -, 50 cycles | 141 |
| ***2. g-C3N4*** | | | | | |

View Article Online
DOI: 10.1039/D4YA00209A

| | | | | | |
|---|---|---|---|---|---|
| $Li_4Ti_5O_{12}$/g-$C_3N_4$ | LIBs-anode | At 0.2 C,174.8 mAh $g^{-1}$ (1C=175 mAh $g^{-1}$) | At 3.2 C, 142.1 mAh $g^{-1}$ | 87 %, 500 cycles | 144 |
| g-$C_3N_4$/$MoS_2$/ZnS | LIBs-anode | At 0.5 A $g^{-1}$, 900 mAh $g^{-1}$ | At 6 A $g^{-1}$, 298 mAh $g^{-1}$ | 99 %, 500 cycles | 145 |
| $MoS_2$/g-$C_3N_4$ | LIBs-anode | At 0.05 C, 2467 mAh $g^{-1}$ (1C=1A $g^{-1}$) | -- | 48 %, 200 cycles | 146 |
| $SnO_2$@$C_3N_4$ | LIBs-anode | 156 mA $g^{-1}$, 995 mAh $g^{-1}$ | 3943 mA $g^{-1}$, 329 mAh $g^{-1}$ | 57 %, 100 cycles | 147 |
| $SnS_2$/g-$C_3N_4$/graphite | LIBs-anode | At 1A $g^{-1}$, 571 mAh $g^{-1}$ | At 5 A $g^{-1}$, 470 mAh $g^{-1}$ | 99.3 %,470 cycles | 148 |
| ZnS/g-$C_3N_4$ | L/SIBs-anode | At 0.1 A $g^{-1}$, 920 mAh $g^{-1}$ (LIB)<br>At 0.1 A $g^{-1}$, 501 mAh $g^{-1}$ (LIB) | At 1 A $g^{-1}$, 612 mAh $g^{-1}$(LIBs)<br>At 0.1 A $g^{-1}$, 920 mAh $g^{-1}$(LIB) | -, 200 cycles<br>-, 100 cycles | 149 |
| $SnS_2$@g-$C_3N_4$ | LIBs-anode | At 50 mA $g^{-1}$, 736 mAh $g^{-1}$ | At 500 mA $g^{-1}$, 736 mAh $g^{-1}$ | -, 600 cycles | 150 |
| $SnO_2$/g-$C_3N_4$ | LIBs-anode | At 0.1 C, 733 mAh $g^{-1}$ | - | -, 60 cycles | 151 |
| $SnO_2$/GO/g-$C_3N_4$ | LIBs-anode | At 0.1 C, 1456 mAh $g^{-1}$ | - | -, 100 cycles | 152 |
| Sn/g-$C_3N_4$ | LIBs-anode | At 100 mA $g^{-1}$, 592 mAh $g^{-1}$ | At 500 mA $g^{-1}$, 420 mAh $g^{-1}$ | 53 %, 100 cycles | 153 |
| $NiCo_2O_4$/g-$C_3N_4$ | LIBs-anode | At 100 mA $g^{-1}$, 1367 mAh $g^{-1}$ | At 1000 mA $g^{-1}$, 452 mAh $g^{-1}$ | 78 %, 100 cycles | 154 |
| CuO@Cu/g-$C_3N_4$ | LIBs-anode | At 0.1 C, 777 mAh $g^{-1}$ | At 2 C, 450 mAh $g^{-1}$ | -, 625 cycles | 155 |
| $MoO_x$/UCN | LIBs-anode | At 0.1 A $g^{-1}$, 1069 mAh $g^{-1}$ | At 2A $g^{-1}$, 703 mAh $g^{-1}$ | 70 %, 100 cycles | 156 |
| g-$C_3N_4$/$WS_2$ | LIBs-anode | At 0.1 C, 655.7 mAh $g^{-1}$ | At 2 C, 247.4 mAh $g^{-1}$ | 68.7 %, 200 cycles | 157 |
| g-$C_3N_4$@RGO | LIBs-anode | At 50 mA $g^{-1}$, 911 mAh $g^{-1}$ | At 800 mA $g^{-1}$, 666 mAh $g^{-1}$ | -, 1000 cycles | 158 |
| P/rGO-$C_3N_4$ | LIBs-anode | At 200 mA $g^{-1}$, 1806 mAh $g^{-1}$ | At 1000 mA $g^{-1}$, 855 mAh $g^{-1}$ | -, 600 cycles | 159 |
| $CuCo_2O_4$@g-$C_3N_4$ | LIBs-anode | At 0.1 A $g^{-1}$, 577 mAh $g^{-1}$ | At 2 A $g^{-1}$, 499 mAh $g^{-1}$ | 76 %, 60 cycles | 160 |
| $Co_{1-x}S$@g-$C_3N_4$ | LIBs-anode | At 0.1 A $g^{-1}$, 789 mAh $g^{-1}$ | -- | -, 210 cycles | 161 |
| Se-H-g-$C_3N_4$ | LIBs-anode | At 0.1 A $g^{-1}$, 814 mAh $g^{-1}$ | At 2 A $g^{-1}$, 544 mAh $g^{-1}$ | 54 %, 1000 cyeles | 162 |
| g-$C_3N_4$/$Mo_2CT_x$ | LIBs-anode | At 0.1 A $g^{-1}$, 606 mAh $g^{-1}$ | At 2 A $g^{-1}$, 257 mAh $g^{-1}$ | 97 %, 1800 cycles | 163 |
| C/g-$C_3N_4$ | SIBs-anode | At 0.1 A $g^{-1}$, 254 mAh $g^{-1}$ | At 1 A $g^{-1}$, 151 mAh $g^{-1}$ | -, 400 cycles | 164 |
| crystalline $C_3N_4$/C | SIBs-anode | At 0.1 A $g^{-1}$, 286 mAh $g^{-1}$ | At 3.2 A $g^{-1}$, 151 mAh $g^{-1}$ | -, 2000 cycles | 165 |



View Article Online
DOI: 10.1039/D4YA00209A

| | | | | | |
|---|---|---|---|---|---|
| Graphite/g-$C_3N_4$ heterojunction | SIBs-anode | At 0.1 A $g^{-1}$, 285 mAh $g^{-1}$ | At 1 A $g^{-1}$, 111 mAh $g^{-1}$ | -, 10000 cycles | 166 |
| $SnS_2$@g-$C_3N_4$ | SIBs-anode | At 50 mA $g^{-1}$, 901 mAh $g^{-1}$ | At 2000 mA $g^{-1}$, 610 mAh $g^{-1}$ | 123 %, 400 cycles | 167 |
| 1D/2D $C_3N_4$/rGO | KIBs-anode | At 0.1 A $g^{-1}$, 464 mAh $g^{-1}$ | | -, 1000 cycles | 168 |
| PCN/rGO | Li-S-cathode | At 0.1 C, 1205 mAh $g^{-1}$ | At 5 C,483 mAh $g^{-1}$ | 61 %, 800 cycles | 190 |
| 3D Porous S/Graphene@g-$C_3N_4$ | Li-S-cathode | At 0.5 C, 1116 mAh $g^{-1}$ | At 5 C, 828 mAh $g^{-1}$ | 86 %, 800 cycles | 191 |
| rGO/g-$C_3N_4$/CNT | Li-S-cathode | At 0.05 C, 1263 mAh $g^{-1}$ | At 2 C, 554 mAh $g^{-1}$ | 85 %, 500 cycles | 192 |
| S/g-$C_3N_4$ | Li-S-cathode | At 0.2 C, 1018 mAh $g^{-1}$ | At 5 C, 607 mAh $g^{-1}$ | 72 %, 300 cycles | 193 |
| g-C3N4/graphene | Li-S-cathode | At 0.2 C, 1098 mAh $g^{-1}$ | At 2 C, 631 mAh $g^{-1}$ | -, 1000 cycles | 194 |
| g-$C_3N_4$/CNT | Li-S-separator | At 0.2 C, 870 mAh $g^{-1}$ | At 2 C, 755 mAh $g^{-1}$ | 85 %, 500 cycles | 196 |
| Fe/Co-C3N4/C/S | Li-S-cathode | At 0.1 C, 1257 mAh $g^{-1}$ | At 2 C, 453 mAh $g^{-1}$ | 78 %, 135 cycles | 197 |
| TixOy-$Ti_3C_2$/$C_3N_4$ | Li-S-cathode | At 0.5 C, 749 mAh $g^{-1}$ | - | 56 %, 2000 cycles | 198 |
| MXene/g-$C_3N_4$ | Li-S-cathode | At 1 C, 718 mAh $g^{-1}$ | At 4 C, 632 mAh $g^{-1}$ | 59 %, 500 cycles | 202 |
| $MoS_2$/g-$C_3N_4$ | Li-S-cathode | At 0.5 C, 925 mAh $g^{-1}$ | At 8 C, 472 mAh $g^{-1}$ | 73 %, 500 cycles | 204 |
| g-$C_3N_4$/g-$C_3N_4$ Heterojunction | Li-S-cathode | At 1 C, 640 mAh $g^{-1}$ | - | 67 %, 150 cycles | 205 |
| Ni-$C_3N_4$/C | Li-S-separator | At 0.1 A $g^{-1}$, 1253 mAh $g^{-1}$ | At 2 A $g^{-1}$, 835 mAh $g^{-1}$ | 89 %, 300 cycles | 206 |
| FeOOH/Coated g-$C_3N_4$/KB | Li-S-separator | At 0.1 C, 1246 mAh $g^{-1}$ | At 2 C, 802 mAh $g^{-1}$ | 50 %, 900 cycles | 207 |
| Co-doped g-$C_3N_4$ | Li-S-separator | At 0.2 C, 1121 mAh $g^{-1}$ | At 2 C, 529 mAh $g^{-1}$ | 95 %, 250 cycles | 208 |
| graphene@g-$C_3N_4$ | Li-O-catalyst | 0.2 mA $cm^{-1}$, 17300 mAh $g^{-1}$ | 0.4 mA $cm^{-1}$, 1000 mAh $g^{-1}$ | -, 105 cycles | 209 |
| Pt@g-$C_3N_4$ | Li-O-catalyst | At 0.2 A $g^{-1}$, 13843 mAh $g^{-1}$ | At 0.8 A $g^{-1}$, 5964 mAh $g^{-1}$ | -, 100 cycles | 215 |
| ***3. MMT*** | | | | | |
| MMT/carbon | LIBs-anode | At 0.02 A $g^{-1}$, 1432 mAh $g^{-1}$ | -- | -, 50 cycles | 220 |
| MCMB@MMT | DIBs-anode | At 2 C, ~ 80 mAh $g^{-1}$ | -- | 100 %, 1000 cycles | 87 |
| MMT/P(VdF-TrFE) | LIBs-separator | At 0.1 C, 119 mAh $g^{-1}$ | At 1 C, 86 mAh $g^{-1}$ | -- | 222 |
| PVDF/MMT | LIBs-separator | At 0.2 C, 138 mAh $g^{-1}$ | At 1 C, 128 mAh $g^{-1}$ | 100 %, 50 cycles | 223 |

View Article Online
DOI: 10.1039/D4YA00209A

| | | | | | |
|---|---|---|---|---|---|
| 5M/P-PMIA | LIBs- gel polymer electrolyte | At 2 C, 140 mAh $g^{-1}$ | -- | 89 %, 200 cycles | 232 |
| MMT@C@PP | Li-S-separator | At 0.5 mA $cm^{-1}$, 1049 mAh $g^{-1}$ | At 3 mA $cm^{-1}$, 684 mAh $g^{-1}$ | 90 %, 300 cycles | 89 |
| Co/N-C@Li-MMT | Li-S-separator | At 0.1 C, 1275 mAh $g^{-1}$ | At 2 C, 656 mAh $g^{-1}$ | -, 100 cycles | 251 |
| MMT/RGP-PP | Li-S-separator | At 0.1 C, 1389 mAh $g^{-1}$ | At 3 C, 848 mAh $g^{-1}$ | 47 % ,800 cycles | 252 |
| PPY/Li-MMT | Li-S-separator | At 0.2 mA $cm^{-1}$, 1226 mAh $g^{-1}$ | At 5 mA $cm^{-1}$, 540 mAh $g^{-1}$ | -, 500 cycles | 253 |
| $FeS_2$@MMT | Li-S-separator | At 0.2 C, 1168 mAh $g^{-1}$ | At 10 C, 358 mAh $g^{-1}$ | 69 %, 1000 cycles | 90 |
| Mmt/carbon black | Li-S-separator | At 0.1 C, 1496 mAh $g^{-1}$ | At 3 C, 541 mAh $g^{-1}$ | 77 %, 500 cycles | 254 |
| $Se_{0.06}$SPAN/MMT@PP | Li-S-separator | At 0.1 C, 1454 mAh $g^{-1}$ | At 5 C, 670 mAh $g^{-1}$ | 66 %, 1000 cycles | 255 |
| ***4. VMT*** | | | | | |
| VMT/PP | LIBs-separator | At 0.1 C, 148 mAh $g^{-1}$ (LFP) | -- | -, 25 cycles | 225 |
| PVDF/VMT/LPT | LIBs-separator | At 0.5 C, 161 mAh $g^{-1}$ (LFP) | -- | 98 %, 100 cycles | 226 |
| PVDF/VMT | LIBs-separator | At 0.2 C, 155 mAh $g^{-1}$ (LFP) | At 2 C, 119 mAh $g^{-1}$ (LFP) | 95%, 100 cycles | 227 |
| 2D vermiculite separator | Li-S-separator | At 0.1 C, 1000 mAh $g^{-1}$ | At 2 C, 600 mAh $g^{-1}$ | -, 50 cycles | 257 |
| Vr/PEO-LCSE | Li-S-SSEs | At 0.05 C, 1252 mAh $g^{-1}$ | At 0.2 C, 1000 mAh $g^{-1}$ | -, 150 cycles | 258 |